10-2016

The bright end of the z~9 and z~10 UV luminosity functions using all five CANDELS fields.

R. J. Bouwens
Leiden University

P. A. Oesch
Yale University

I. Labbe
Leiden University

G. D. Illingworth
University of California, Santa Cruz

G. G. Fazio
Harvard-Smithsonian Center for Astrophysics

See next page for additional authors

Authors

R. J. Bouwens, P. A. Oesch, I. Labbe, G. D. Illingworth, G. G. Fazio, D. Coe, Benne W. Holwerda, R. Smit, M. Stefanon, P. G. van Dokkum, M. Trenti, M. L. N. Ashby, J. S. Huang, L. Spitler, C. Straatman, L. Bradley, and D. Magee

THE BRIGHT END OF THE $z \sim 9$ AND $z \sim 10$ UV LUMINOSITY FUNCTIONS USING ALL FIVE CANDELS FIELDS[*]

R. J. BOUWENS[1], P. A. OESCH[2], I. LABBÉ[1], G. D. ILLINGWORTH[3], G. G. FAZIO[4], D. COE[5], B. HOLWERDA[1], R. SMIT[6], M. STEFANON[1], P. G. VAN DOKKUM[2], M. TRENTI[7], M. L. N. ASHBY[4], J.-S. HUANG[4], L. SPITLER[8], C. STRAATMAN[1], L. BRADLEY[5], AND D. MAGEE[3]

[1] Leiden Observatory, Leiden University, NL-2300 RA Leiden, The Netherlands
[2] Department of Astronomy, Yale University, New Haven, CT 06520, USA
[3] UCO/Lick Observatory, University of California, Santa Cruz, CA 95064, USA
[4] Harvard-Smithsonian Center for Astrophysics, Cambridge, MA, USA
[5] Space Telescope Science Institute, 3700 San Martin Drive, Baltimore, MD 21218, USA
[6] Department of Physics and Astronomy, South Road, Durham, DH1 3EE, UK
[7] School of Physics, The University of Melbourne, VIC 3010, Australia
[8] Department of Physics & Astronomy, Macquarie University, Sydney, NSW 2109, Australia

ABSTRACT

The deep, wide-area ($\sim$800–900 arcmin^2) near-infrared/WFC3/IR + *Spitzer*/IRAC observations over the CANDELS fields have been a remarkable resource for constraining the bright end of high-redshift UV luminosity functions. However, the lack of *Hubble Space Telescope* (*HST*) 1.05 μm observations over the CANDELS fields has made it difficult to identify $z \sim 9$–10 sources robustly, since such data are needed to confirm the presence of an abrupt Lyman break at 1.2 μm. Here, we report on the successful identification of many such $z \sim 9$–10 sources from a new *HST* program (z9-CANDELS) that targets the highest-probability $z \sim 9$–10 galaxy candidates with observations at 1.05 μm, to search for a robust Lyman-break at 1.2 μm. The potential $z \sim 9$–10 candidates were preselected from the full *HST*, *Spitzer*/IRAC S-CANDELS observations, and the deepest-available ground-based optical+near-infrared observations (CFHTLS-DEEP+HUGS+UltraVISTA+ZFOURGE). We identified 15 credible $z \sim 9$–10 galaxies over the CANDELS fields. Nine of these galaxies lie at $z \sim 9$ and five are new identifications. Our targeted follow-up strategy has proven to be very efficient in making use of scarce *HST* time to secure a reliable sample of $z \sim 9$–10 galaxies. Through extensive simulations, we replicate the selection process for our sample (both the preselection and follow-up) and use it to improve current estimates for the volume density of bright $z \sim 9$ and $z \sim 10$ galaxies. The volume densities we find are $5^{+3}_{-2}\times$ and $8^{+9}_{-3}\times$ lower, respectively, than those found at $z \sim 8$. When compared with the best-fit evolution (i.e., $d \log_{10} \rho_{\mathrm{UV}}/dz = -0.29 \pm 0.02$) in the UV luminosity densities from $z \sim 8$ to $z \sim 4$ integrated to $0.3L^{*}_{z=3}$ (-20 mag), these luminosity densities are $2.6^{+1.5}_{-0.9}\times$ and $2.2^{+2.0}_{-1.1}\times$ lower, respectively, than the extrapolated trends. Our new results are broadly consistent with the "accelerated evolution" scenario at $z > 8$, consistent with that seen in many models.

Key words: galaxies: formation – galaxies: high-redshift

1. INTRODUCTION

The first galaxies are thought to have formed in the first 300–400 Myr of the universe. Over the last few years, remarkable progress has been made in extending samples back to this time, with more than $\sim$700 probable galaxies identified at $z \gtrsim 6.3$ with the *Hubble Space Telescope* (*HST*; McLure et al. 2013; Bouwens et al. 2015; Finkelstein et al. 2015) and 20–30 candidate galaxies identified as far back as redshifts $z \sim 9$–11 (Bouwens et al. 2011a, 2014a, 2015; Zheng et al. 2012; Coe et al. 2013; Ellis et al. 2013; McLure et al. 2013; Oesch et al. 2013, 2014, 2015; Zitrin et al. 2014; Ishigaki et al. 2015; McLeod et al. 2015).

At present and over the next year, considerable resources are being devoted to both the discovery and study of ultra-faint galaxies with *HST* from the new Frontier Fields initiative (e.g., Lotz et al. 2014; Coe et al. 2015).[9] The goal of this initiative is to combine the power of gravitational lensing from galaxy clusters with very deep exposures with the *Hubble* and *Spitzer Space Telescopes*. Eight hundred forty orbits of *HST*

observations are being invested in deep optical/ACS + near-IR/WFC3/IR observations of six galaxy clusters. Deep observations of a "blank" field outside the galaxy clusters are also being obtained in parallel with observations over the clusters.

Despite the considerable focus by the community on the Hubble Frontier Fields observations over galaxy clusters and deep fields (e.g., Atek et al. 2014, 2015; Zheng et al. 2014; Coe et al. 2015; Ishigaki et al. 2015; Oesch et al. 2015), it is also possible to uncover modest numbers of luminous $z \sim 9$–10 galaxies over wide-field surveys, as first illustrated by Oesch et al. (2014) through the identification of six intrinsically luminous $z \sim 9$–10 candidate galaxies over the GOODS-North and GOODS-South CANDELS fields (Grogin et al. 2011; Koekemoer et al. 2011). These sources allowed us to set some initial constraints on the rate at which UV-luminous galaxies evolve with cosmic time, and provided some constraints on the approximate shape of the UV luminosity functions (LFs) at $z = 9$–10.

Due to the inherent brightness of such sources, these sources are also valuable for efforts to measure the physical properties of galaxies at very early times. Measurements of the UV-continuum slopes (Oesch et al. 2014; Wilkins et al. 2016), Balmer-break amplitudes (Oesch et al. 2014), stellar masses

---

[9] http://www.stsci.edu/hst/campaigns/frontier-fields/

Table 1
Observational Data Used to Identify[a] the Bright $z \sim 9$–10 Candidate Galaxies over the CANDELS UDS, COSMOS, and EGS Fields[*]

|								
Two-part Search Strategy (Preselection + Follow-up: Sections 3, 4)								
CANDELS UDS			**CANDELS COSMOS**			**CANDELS EGS**		
Filter[a]	5σ Depth[b]	Source	Filter[a]	5σ Depth[b]	Source	Filter[a]	5σ Depth[b]	Source
V_{606}	26.8	HST/ACS	V_{606}	26.5	HST/ACS	V_{606}	27.3	HST/ACS
I_{814}	26.8	HST/ACS	I_{814}	26.5	HST/ACS	I_{814}	27.1	HST/ACS
J_{125}	26.3	HST/WFC3	J_{125}	26.1	HST/WFC3	J_{125}	26.4	HST/WFC3
JH_{140}	26.1	HST/WFC3	JH_{140}	25.8	HST/WFC3	JH_{140}	25.6	HST/WFC3
H_{160}	26.5	HST/WFC3	H_{160}	26.3	HST/WFC3	H_{160}	26.6	HST/WFC3
u	25.8	CFHT/Megacam	u	27.7	CFHT/Megacam	u	27.4	CFHT/Megacam
B	28.0	Subaru/Suprime-Cam	$B + g$	28.4	Subaru/Suprime-Cam +	g	27.8	CFHT/Megacam
$V + r$	28.0	Subaru/Suprime-Cam			CFHT/Megacam	r	27.6	CFHT/Megacam
i	27.4	Subaru/Suprime-Cam	$V + r$	27.9	Subaru/Suprime-Cam +	$i + y$	27.4	CFHT/Megacam
z	26.3	Subaru/Suprime-Cam			CFHT/Megacam	z	26.0	CFHT/Megacam
Y	25.9	VLT/HAWKI/HUGS	$i + y$	27.7	Subaru/Suprime-Cam +	K	24.1	UKIRT/WIRCam
J_1	25.6	Magellan/FOURSTAR			CFHT/Megacam	3.6 μm	25.4	Spitzer/S-CANDELS
J_2	25.7	Magellan/FOURSTAR	z	26.4	Subaru/Suprime-Cam +	4.5 μm	25.3	Spitzer/S-CANDELS
J	25.4	UKIRT/WFCAM			CFHT/Megacam			
J_3	25.4	Magellan/FOURSTAR	Y	26.1	UltraVISTA			
H	24.6	UKIRT/WFCAM	J_1	25.6	Magellan/FOURSTAR			
H_s	25.0	Magellan/FOURSTAR	J_2	25.5	Magellan/FOURSTAR			
H_l	24.8	Magellan/FOURSTAR	J	25.3	UltraVISTA			
K_s	25.5	VLT/HAWKI/HUGS +	J_3	25.3	Magellan/FOURSTAR			
		UKIRT/WFCAM +	H_s	24.7	Magellan/FOURSTAR			
		Magellan/FOURSTAR	H	25.0	UltraVISTA			
			H_l	24.7	Magellan/FOURSTAR			
			K_s	25.3	UltraVISTA +			
					Magellan/FOURSTAR			
3.6 μm	25.4	Spitzer/S-CANDELS	3.6 μm	25.3	Spitzer/S-CANDELS			
4.5 μm	25.4	Spitzer/S-CANDELS	4.5 μm	25.3	Spitzer/S-CANDELS			
Direct Search Strategy for $z \geqslant 8.4$ Galaxies (Section 5)								
CANDELS GOODS-South			**ERS**			**CANDELS GOODS-North**		
B_{435}	27.1–27.3	HST/ACS	B_{435}	27.1	HST/ACS	B_{435}	27.2–27.3	HST/ACS
V_{606}	27.4–27.7	HST/ACS	V_{606}	27.4	HST/ACS	V_{606}	27.4	HST/ACS
$i_{775}+$			$i_{775}+$			$i_{775}+$		
I_{814}	27.5–27.6	HST/ACS	I_{814}	27.3	HST/ACS	I_{814}	27.2–27.7	HST/ACS
z_{850}	26.8–26.9	HST/ACS	z_{850}	26.7	HST/ACS	z_{850}	26.9–27.0	HST/ACS
Y_{105}	26.4–27.0	HST/WFC3	Y_{098}	26.5	HST/WFC3	Y_{105}	26.5–26.8	HST/WFC3
J_{125}	26.5–27.0	HST/WFC3	J_{125}	27.0	HST/WFC3	J_{125}	26.4–27.2	HST/WFC3
JH_{140}	26.1	HST/WFC3	JH_{140}	25.8	HST/WFC3	JH_{140}	25.6	HST/WFC3
H_{160}	26.5–27.0	HST/WFC3	H_{160}	26.9	HST/WFC3	H_{160}	26.5–27.1	HST/WFC3
K_s	26.5	VLT/HAWKI/HUGS +	K_s	26.5	VLT/HAWKI/HUGS +			
		VLT/ISAAC +			VLT/ISAAC +			
		PANIC +			PANIC +			
		Magellan/FOURSTAR			Magellan/FOURSTAR			
3.6 μm	25.8	Spitzer/S-CANDELS	3.6 μm	25.8	Spitzer/S-CANDELS	3.6 μm	25.8	Spitzer/S-CANDELS
4.5 μm	25.8	Spitzer/S-CANDELS	4.5 μm	25.8	Spitzer/S-CANDELS	4.5 μm	25.8	Spitzer/S-CANDELS

Notes.
[a] For each source in our search fields, flux measurements are derived based on all of the observational data presented in this table. All of these measurements are used in deriving a redshift likelihood distribution for individual sources.
[b] The 5σ depths are estimated from the median 5σ uncertainties on the total flux measurements of sources found over our search fields with $H_{160,AB}$-band magnitudes of 26.0–26.5.

(Oesch et al. 2014), and sizes (Holwerda et al. 2015; Shibuya et al. 2015) can all be achieved using very bright galaxies.

Despite the usefulness of bright $z \sim 9$–10 galaxies for addressing many contemporary science questions, current samples of these objects remain quite small and constraints on their volume densities are poor. Of particular note is that the

recent Oesch et al. (2014) sample over the GOODS-North and GOODS-South fields only contained 2 bright $z \sim 9$ and 4 bright $z \sim 10$ galaxies. With such small samples, current uncertainties on the volume density of bright $z \sim 9$–10 galaxies are large indeed ($\gtrsim 0.3$–0.4 dex). This is especially the case when one considers the impact of field-to-field variations ("cosmic
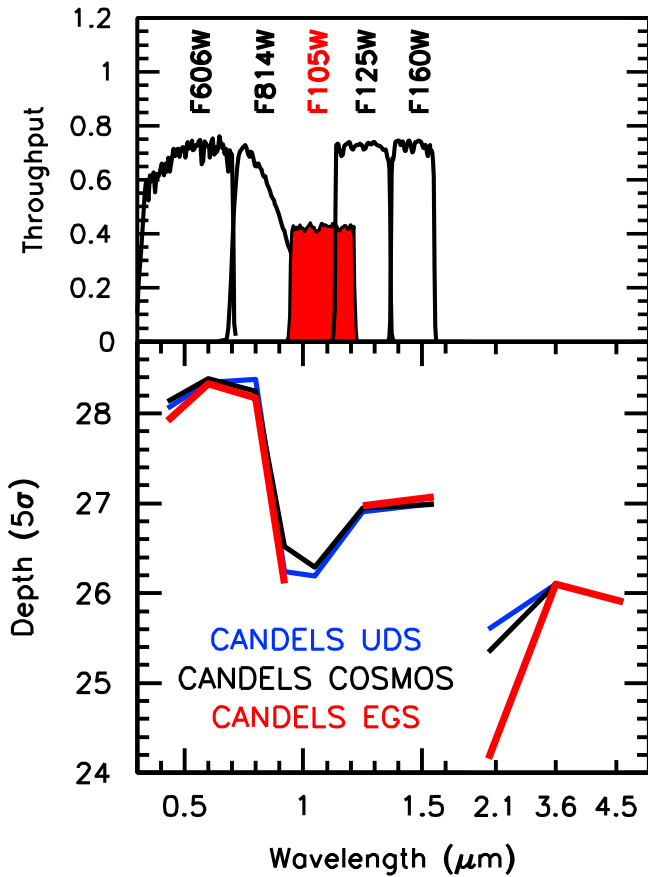
Figure 1. (Upper panel) Wavelength sensitivity curves for the filters (F606W, F814W, F125W, F160W) in which deep *HST* observations are available over the CANDELS UDS, COSMOS, and EGS fields (black), as well as those (F105W) primarily obtained by our follow-up program z9-CANDELS (red). (Lower panel) 5σ median depths of the observations vs. wavelength available over the CANDELS UDS, COSMOS, and EGS fields (see also the compilations in Table 1 and Figure 2 of Bouwens et al. 2015). The depths plotted here are binned in such a way as to combine all of the data (Table 1) that exist in 0.1–0.15 μm segments. The depths do not include the ZFOURGE observations here, since those observations only cover $\gtrsim$65% of each CANDELS field (adding some useful depth from 1.0 to 1.7 μm). There is a modest wavelength gap between the deeper observations at $\sim$0.6–0.9 μm and those which exist at $\sim$1.2–1.6 μm. While some ($\sim$26 mag, 5σ) observations exist at 1.05 μm to probe below the putative Lyman-break for $z \sim$ 9–10 galaxy candidates, the addition of deep observations at 1 μm with *HST* can significantly improve current constraints on the robustness of the Lyman-break at 1 μm.

break, distinguishing such galaxies from dusty, red galaxies at $z \sim$ 1–3. While possessing great potential, the CANDELS UDS, COSMOS, and EGS search areas lack correspondingly deep observations at 1.05 μm, just blueward of the Lyman-break in candidate $z \sim$ 9–10 galaxies, which is important for confirming a spectral break at $\sim$1.2 μm and distinguishing these $z \gtrsim$ 9 galaxy candidates from Balmer-break sources at $z \sim$ 1–3.

Fortunately, we can overcome the aforementioned limitations of the CANDELS UDS, COSMOS, and EGS data sets by leveraging essentially all of the existing observations over these fields (Table 1) to first identify the highest-probability $z \sim$ 9–10 candidates over these fields and then obtaining targeted follow-up observations of these candidates at 1.05 μm to determine which are likely at $z >$ 8 (Figure 1). In cycle 21, we successfully proposed such a follow-up program of plausible candidate $z \sim$ 9–10 galaxies over the CANDELS UDS, COSMOS, and EGS fields. Observations from this program—which we call z9 (redshift 9)-CANDELS (Bouwens 2014: GO 13792)—are now complete and cover all 12 of the primary candidates from that program. Based on the information we obtained from our proposed follow-up observations and the selection criteria we used in identifying our initial sample of 12 candidate $z \sim$ 9–10 galaxies from these three CANDELS fields, we can derive constraints on the volume density of luminous $z \sim$ 9–10 galaxies. Searches over CANDELS-GOODS-North, CANDELS-GOODS-South, the ERS fields can be further used to improve the constraints we obtain on the bright end of the $z \sim$ 9–10 LFs.

In this paper, we describe (1) the preselection we used to identify candidate $z \sim$ 9–10 galaxies from the CANDELS-UDS, COSMOS, and EGS fields for *HST* follow-up observations and (2) the results from this program. Our primary scientific objective is to obtain the best available constraints on the volume density of especially luminous $z \sim$ 9 and $z \sim$ 10 galaxies. Through such constraints, we have a direct measure of how fast (1) the bright end of the UV LF and (2) UV-luminous galaxies evolve. Through comparison with the volume density of fainter sources, the present search results also allow us to constrain the overall shape of the UV LF. Finally, we would expect our selection to allow us to considerably expand the overall sample of bright $z \sim$ 9 and $z \sim$ 10 galaxies available over the CANDELS fields. This has value both for the further characterization of the physical properties of $z \gtrsim$ 9 galaxies and as bright sources to target with early *James Webb Space Telescope* observations. These bright samples will be further enhanced with bright $z \sim$ 9–10 galaxies from the BoRG[$_{z910}$] program (Trenti 2014).

Here, we present a brief plan for this paper. In Section 2, we include a description of the observational data that we use to identify high-probability $z \sim$ 9–10 galaxies over the CAN-DELS-UDS, COSMOS, and EGS fields. In Section 3, we describe our criteria for performing photometry and identifying high-probability $z \sim$ 9–10 galaxy candidates over the CANDELS-UDS, COSMOS, and EGS fields. In Section 4, we describe the results of the z9-CANDELS program where we use these observations to ascertain the likely nature of our selected $z \sim$ 9–10 candidate galaxies. In Section 5, we describe our search results for bright $z \gtrsim$ 8.4 candidate galaxies over the CANDELS GOODS-North, GOODS-South fields, and ERS fields, extending previous work by Oesch et al. (2014: see also McLure et al. 2013 who also conducted such a search over the GOODS-South field). Finally, in Section 6, we make use of these search results to provide the first constraints on the bright

variance"), which is as large as a factor of two across the CANDELS fields, e.g., see Figure 14 from Bouwens et al. (2015), and may be even larger for the brightest sources (Bowler et al. 2015; Roberts-Borsani et al. 2016). Clearly, we require many independent lines of sight to the $z \sim$ 9–10 universe to average over the large-scale structure. Unfortunately, the Frontier Fields Initiative will not significantly help with this issue for luminous sources, given the limited area covered by observations from this program.

Nevertheless, there is a huge quantity of *HST* and *Spitzer* data already available that can be used to construct larger samples of bright $z \sim$ 9–10 galaxies. The most significant of these data sets are the $\sim$500 arcmin^2 CANDELS UDS, COSMOS, and EGS fields which feature very deep optical, near-IR, and *Spitzer*/IRAC observations. These observations are very useful for the robust detection of bright $z \sim$ 9–10 candidates and also to confirm a blue color redward of the

end of the $z \sim 9$ and $z \sim 10$ LFs using a search over all five CANDELS fields.

For consistency with previous work, we quote results in terms of the luminosity $L_{z=3}^{*}$ derived by Steidel et al. (1999) at $z \sim 3$, i.e., $M_{1700,AB} = -21.07$. We refer to the *HST* F435W, F606W, F775W, F814W, F850LP, F098M F105W, F125W, F140W, and F160W bands as B_{435}, V_{606}, i_{775}, I_{814}, z_{850}, Y_{098}, Y_{105}, J_{125}, JH_{140}, and H_{160}, respectively, for simplicity. Where necessary, we assume $\Omega_0 = 0.3$, $\Omega_\Lambda = 0.7$, and $H_0 = 70$ km s^{-1} Mpc^{-1}. All magnitudes are in the AB system (Oke & Gunn 1983).

2. OBSERVATIONAL DATA

In the present analysis, we conduct a search for bright $z \sim$ 9–10 candidate galaxies over the $\sim$450 arcmin^2 region within the CANDELS-UDS, COSMOS, and EGS fields with the deepest *HST* optical/ACS and near-IR/WFC/IR observations ($\sim$75%–80% of the WFC3/IR area).

In conducting this search, we use the reductions of the *HST* observations described in Bouwens et al. (2015). Those reductions include all observations associated with the AEGIS, COSMOS, and CANDELS *HST* surveys and SNe follow-up programs, including the JH_{140}-band observations associated with the 3D-*HST* (Brammer et al. 2012) and AGHAST (Weiner et al. 2014) programs.

Beyond the *HST* observations themselves, perhaps the most valuable data set that we can leverage in our search for probable $z \sim 9$–10 galaxies is the very deep *Spitzer*/IRAC S-CANDELS observations over the CANDELS fields (Ashby et al. 2015) which, when combined with *Spitzer*/IRAC SEDS observations (Ashby et al. 2013), reach 50 hr in depth (26.0 mag at 5σ: 2″-diameter apertures). Those observations provide us with constraints on the spectral slope of galaxies redward of the H_{160} band which, when combined with evidence for a break across the J_{125} and H_{160} bands and a non-detection at optical wavelengths, is strongly suggestive of a $z \sim 9$–10 galaxy.

In addition, we also make use of all significant, public ground-based observations over these fields, including optical observations from Subaru Suprime-Cam [CANDELS-COSMOS; CANDELS-UDS] and CFHT/Megacam [CANDELS-COSMOS; CANDELS-EGS], and deep near-IR observations from VISTA [CANDELS-COSMOS], UKIRT/WFCAM [CANDELS-UDS], VLT/HAWKI [CANDELS-UDS], *Magellan*/FOURSTAR [CANDELS-COSMOS; CANDELS-UDS], and CFHT/WIR-Cam [CANDELS-EGS]. The deep optical observations allow us to search for faint optical flux in the $z \sim 9$–10 candidates identified over the CANDELS-UDS/COSMOS/EGS fields, while the near-IR observations allow us to test for the presence of a putative break at 1.2 μm, to verify that candidates show no flux blueward of the break, and to test for a flat UV-continuum redward of the break.

In our analysis of data over the five CANDELS fields and the $\sim$40 arcmin^2 ERS field (Windhorst et al. 2011), we use the Bouwens et al. (2015) reductions of the *HST* observations over all five CANDELS fields, the version 7 reduction of the deep CFHT legacy survey observations over the COSMOS and EGS fields,[10] the public v2.0 reductions of the UltraVISTA observations (McCracken et al. 2012), the Cirasuolo et al. (2010) redutions of the deep Subaru Suprime-Cam observations over the UDS/SXDS field (Furusawa et al. 2008), the

Bouwens et al. (2015) reductions of the HUGS HAWK-I observations (Fontana et al. 2014), the public reductions of the WIRCam deep survey K_s-band observations over the CANDELS EGS field (McCracken et al. 2010; Bielby et al. 2012), the v0.9.3/v0.95.5 reductions of the ZFOURGE COSMOS/UDS observations (I. Labbé et al. 2015, in preparation), the IUDF reductions of the *Spitzer*/IRAC observations over the GOODS-South and GOODS-North fields (Labbé et al. 2015), and the public reductions of the *Spitzer* SEDS and S-CANDELS programs (Ashby et al. 2013, 2015).

Table 1 provides a convenient summary of all of the observational data we use. Combining the flux measurements from the different data sets, the 5σ depths of these fields (derived from the median uncertainties on the total flux measurements) range from $\sim$28 mag at <0.8 μm, $\sim$26.0–26.5 mag at $\sim$0.9 μm, $\sim$26.0 mag at 1.05 μm, $\sim$26.6 mag at $\sim$1.2–1.6 μm, 24.1–25.5 mag at 2.3 μm, to 25.6–25.9 mag at 3.6 μm + 4.5 μm. We refer interested readers to Figure 3 from Bouwens et al. (2015) for a graphical representation of these depths as a function of wavelength.

3. $z \sim 9$–10 SELECTION

3.1. Catalog Construction and Photometry

As in previous work (e.g., Bouwens et al. 2007, 2011b, 2015), we use a modified version of the SExtractor software (Bertin & Arnouts 1996) to construct our *HST* source catalogs that lie at the core of our $z \sim 9$–10 selection. SExtractor is run in dual mode, with source detection performed with the H_{160}-band images and photometry performed on the V_{606}, I_{814}, J_{125}, JH_{140}, and H_{160} images one at a time. Color measurements are made in small scalable apertures using Kron-style (1980) photometry and a Kron parameter of 1.2. Fluxes measured in these small scalable apertures are then corrected to total in two steps. In the first step, we multiply each of the fluxes by the excess flux seen in the larger scalable apertures (Kron parameter of 2.5) for the H_{160}band over that present in smaller scalable apertures. In the second step, we correct for the light on the wings of the point-spread function (PSF) and outside our larger scalable apertures based on the tabulated encircled energy corrections for point sources (Dressel et al. 2012).

For measurements of the flux in the ground-based observations or the *Spitzer*/IRAC observations, we use the MOPHONGO software (Labbé et al. 2006, 2010a, 2010b, 2013, 2015). This software allows us to cope with the significant amounts of overlap in the light distribution for nearby sources. As with other software in the literature with similar objectives, MOPHONGO attempts to overcome the issue of source confusion by assuming that the high-resolution *HST* images (here the H_{160}-band image) provide an accurate model of the spatial profile of sources in the ground-based/*Spitzer*/IRAC images, and that only the normalization of the source flux varies from one passband to another. MOPHONGO then varies their individual fluxes to obtain a good fit. Measurements of the flux for individual sources are then performed in fixed circular apertures after subtracting the model light profile from neighboring sources. We use 1″.2-diameter, 1″.8-diameter, and 2″-diameter apertures for the ground-based photometry, *Spitzer*/IRAC, and *Spitzer*/IRAC photometry over all of our fields, the CANDELS GOODS-North+GOODS-South fields, and the CANDELS UDS/COSMOS/EGS fields. The measured fluxes are then corrected to the total based on the model

---

[10] http://www.cfht.hawaii.edu/Science/CFHTLS
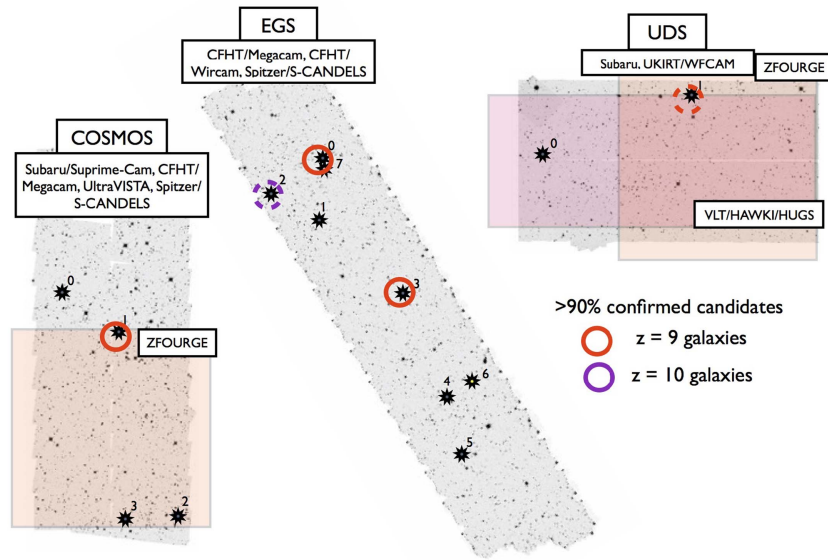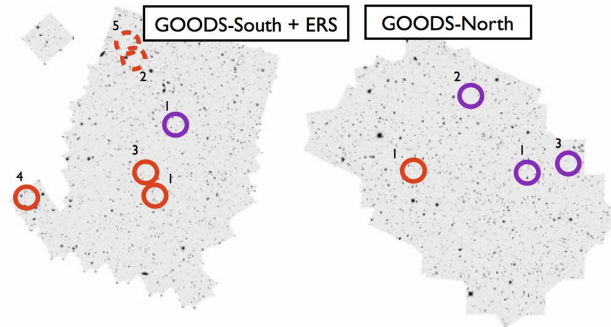
Figure 2. H_{160}-band images of the CANDELS-UDS, COSMOS, and EGS search data that we used to identify tentative candidate $z \sim 9$–10 galaxies. The positions of the candidate $z \sim 9$–10 sources are indicated by the stars on these mosaics. The numbers adjacent to the stars indicate the identity of the tentative $z \sim 9$–10 candidate (identical the numbering scheme employed in Table 3). Those stars shaded in gray indicate sources that were explicitly preselected for targeted follow-up observations from our 11-orbit z9-CANDELS program, while those shaded in yellow were not preselected and only incidentally targeted (lowest two rows in Table 3). Also shown are the regions within these fields where deep near-IR observations are available from programs like HUGS (Fontana et al. 2014) or ZFOURGE (I. Labbé et al. 2015, in preparation), which cover most but not all of the area over the targeted CANDELS fields. The candidates enclosed in red or purple circles appear very likely (>90% confidence) to be at $z \sim 9$ or $z \sim 10$, respectively, based on the available photometric constraints (obtained with our *HST* follow-up program or archival observations).

profile for individual sources. Narrower apertures are used for our *Spitzer*/IRAC photometry over the GOODS-North+ GOODS-South fields to leverage the narrower FWHM of the *Spitzer*/IRAC PSF in the Labbé et al. (2015) reductions.

3.2. Selection of Bright $z \sim 9$–10 Candidates over the CANDELS-UDS and CANDELS-COSMOS Fields

3.2.1. Selection Criteria

In searching for candidate galaxies at $z \sim 9$–10, we suppose that these galaxies have colors and SEDs very similar to galaxies at slightly lower redshifts. Specifically, we would expect these sources to show a sharp spectral break at 1216 Å due to strong absorption from the neutral hydrogen forest, and to exhibit a blue UV-continuum redward of the break.

For star-forming galaxies at redshifts $z \sim 8.4$ and higher, the Lyman-break will already have redshifted a significant way

through the J_{125}-band, yielding moderately red $J_{125} - H_{160}$ colors. As a result, the selection of all sources with red $J_{125} - H_{160}$ colors should allow us to identify the bulk of star-forming galaxies from $z \sim 8.7$ to $z \sim 11$ (particularly if those galaxies are not substantially dust obscured).

Here, we search for candidate $z \gtrsim 8.4$ galaxies over the CANDELS-UDS and COSMOS fields using a $J_{125} - H_{160} > 0.5$ criterion. Star-forming galaxies with a UV-continuum slope β of -1.6 (typical of luminous galaxies at $z = 4$–7) would have a $J_{125} - H_{160}$ color of ~ 0.5 at $z = 8.7$, but the lower-redshift limit for our selection will depend on the intrinsic colors of individual galaxies and also can be affected by observational noise.

In addition to our $J_{125} - H_{160}$ criterion, we also require that sources be undetected ($<2\sigma$) in the V_{606} or I_{814} bands. Sources where the root mean square signal-to-noise ratio (S/N) in the V_{606} and I_{814} bands is greater than 1 are excluded. In addition to these non-detection requirements on the *HST* optical data, we

also require that sources remain undetected ($<2.5\sigma$) in an inverse-variance-weighted mean stack of the ground-based optical data.

We also demand that sources show $H_{160} - [3.6]$ colors bluer than 1.4 mag to exclude intrinsically red or old $z \sim 2$ galaxies from our samples, similar to the criteria applied by Oesch et al. (2014) or Bouwens et al. (2015). This particular color cut corresponds to a UV-continuum slope β of 0.0 (where $f_\lambda \propto \lambda^\beta$), which is approximately as red as bright galaxies are observed to be at $z \sim 6$–8 (e.g., Wilkins et al. 2011; Bouwens et al. 2012, 2014b; Finkelstein et al. 2012; Rogers et al. 2014).

We require that all selected $z \sim 9$–10 candidates show strong evidence of correspondence to real sources. We therefore require that (1) sources be detected in the H_{160} band at $>5\sigma$ significance, (2) the root mean square detection significance of sources in the JH_{140}- and H_{160}-band images be at least 6, and (3) the root mean square detection significance of sources in the JH_{140}, [3.6], [4.5], and K bands be at least 2σ.

Finally, in the last step, we compute the redshift likelihood distribution for each candidate source using the EAZY photometric redshift code (Brammer et al. 2008) based on the photometry we have available for sources, the standard EAZY_v1.0 template set, and a flat prior. We supplemented the standard EAZY_v1.0 template set with SED templates from the Galaxy Evolutionary Synthesis Models (Kotulla et al. 2009). Nebular continuum and emission lines were added to the later templates using the Anders & Fritze-v. Alvensleben (2003) prescription, a $0.2\,Z_\odot$ metallicity, and a rest-frame EW for Hα of 1300 Å (which appears to be appropriate for $z \sim 6$–7; Smit et al. 2014, 2015; Roberts-Borsani et al. 2016).

The photometry used for constraining the likelihood distributions for individual sources included the *HST* $V_{606}I_{814}J_{125}JH_{140}H_{160}$ + Subaru-SuprimeCam *BgVriz* + CFHT/Megacam *ugriyz* + UltraVISTA *YJHK$_s$* + ZFOURGE $J_1J_2J_3H_sH_l$ + *Spitzer*/IRAC $3.6\,\mu$m + $4.5\,\mu$m S-CANDELS data sets for the CANDELS COSMOS field, *HST* $V_{606}I_{814}J_{125}JH_{140}H_{160}$ + Subaru-SuprimeCam *BVriz* + CFHT/Megacam *u* + UKIRT/WFCAM *JHK$_s$* + ZFOURGE $J_1J_2J_3H_sH_l$ + VLT/HAWKI/HUGS *YK$_s$* data sets for the CANDELS UDS field, and the *HST* $V_{606}I_{814}J_{125}JH_{140}H_{160}$ + CFHT/Megacam *ugriyz* + CFHT/WIRCam *K$_s$* + *Spitzer*/IRAC $3.6\,\mu$m+$4.5\,\mu$m data sets for the CANDELS EGS field. The depths of these observations are provided in Table 1 and their areal coverage is illustrated in Figure 2.

Sources that satisfied our aforementioned criteria, which showed a $>50\%$ probability of being at $z > 8$, and which could be confirmed to be a $>90\%$ likelihood candidate with a single orbit of follow-up observations (supposing sources are measured to have a flux of 0 ± 12 nJy in the Y_{105} band), made it into our final preselection of candidate $z \sim 9$–10 galaxies (to be targeted with follow-up observations). In computing the posterior probability that a source has a redshift of $z > 8$ or $z < 8$, we adopt a flat prior on the redshift.

Table 2 provides a convenient compilation of all of the selection criteria we employed in preselecting candidate $z \sim 9$–10 galaxies to follow-up with targeted observations.

3.2.2. UDS+COSMOS Results

Applying the selection criteria from the previous section to our source catalogs over the CANDELS-UDS and CANDELS-COSMOS fields, we found five sources which satisfied all of the criteria. A list of all 6 sources satisfying these criteria are included in Table 3 along with similar candidates from the CANDELS-EGS field.

The observed spectral energy distributions for these five candidate $z \sim 9$–10 galaxies are presented in Appendix A (Figure 11), along with SED fits to a model $z > 8$ galaxy and a model $z < 3$ galaxy. Also shown in this figure is the redshift likelihood distribution (*solid black line*) based on the photometry we have available for each candidate in the $\sim$20 different wavelength channels (*HST* + *Spitzer*/IRAC + ground-based observations). In addition, this figure presents the redshift likelihood distribution we would expect assuming that these candidates are not detected in the single orbit of follow-up Y_{105}-band observations from the z9-CANDELS program.

Postage stamp images of these six candidates are also presented in Appendix A (Figure 10). As should be obvious from this figure, all six of the present $z \sim 9$–10 candidates show clear detections in the H_{160} band, as well as significant $\sim$2–3σ detections in the J_{125}-band and JH_{140}-band observations (where available), as well as in the S-CANDELS *Spitzer*/IRAC data.

All six of these candidates bear a remarkable similarity to the first samples of particularly luminous $z \sim 9$–10 galaxies identified by Oesch et al. (2014) in terms of their very blue $H_{160} - [3.6]$ colors (see also Wilkins et al. 2016), red [3.6]–[4.5] colors, and observed sizes (Holwerda et al. 2015).

3.3. Selection of $z \sim 9$–10 Candidates Over the CANDELS-EGS

3.3.1. Selection Criteria

The selection of candidate $z \sim 9$–10 galaxies over the CANDELS-EGS field is even more challenging than selection over the CANDELS-UDS and CANDELS-COSMOS fields due to the lack of deep observations at 1.05 μm over the CANDELS-EGS field. Y-band observations (at 1.05 μm) play a crucial role in excluding the possibility that sources can correspond to slightly reddened star-forming galaxies at $z \sim 7.5$–8.5 or to passive or reddened galaxies at much lower redshifts.

In selecting $z \sim 9$–10 candidates over the CANDELS-EGS field, we therefore adopted almost identical criteria as for the CANDELS-COSMOS or CANDELS-UDS fields, with one exception. Instead of requiring sources to have a $>50\%$ probability of corresponding to a $z > 8$ galaxy, we required that sources be capable of confirmation with a single orbit of *HST* observations at 1.05 μm. For the purpose of selection, our confirmation corresponds to the source having $>90\%$ likelihood of being at $z > 8$ after adding a flux constraint of 0 ± 12 nJy to the observed SED at 1.05 μm (although we obtained follow-up observations in JH_{140} for the one case where the $J_{125} - H_{160}$ color was >1.2).

3.3.2. EGS Results

Applying the selection criteria from the previous section to our source catalogs over the CANDELS-EGS field, we found six additional sources which satisfied all of the criteria (Table 3).

The observed spectral energy distributions for these six candidate $z \sim 9$–10 galaxies are presented in Appendix A (Figure 11), along with SED fits to a model $z > 6$ galaxy and a model $z < 6$ galaxy. Postage stamp images of these six candidate $z \sim 9$–10 galaxies are also provided.

Table 2
Selection Criteria Used in Assembling Our $z \sim 9$ and $z \sim 10$ Samples

Redshift Sample	Selection Criteria	
	Preselection for Targeted *HST* Follow-up	After *HST* Follow-up
	CANDELS-UDS + CANDELS-COSMOS	
9	$(J_{125} - H_{160} > 0.5) \wedge (H_{160} - [3.6] < 1.4) \wedge (\text{S/N in both } V_{606} \text{ and } I_{814} < 2) \wedge$ (rms S/N in V_{606} and $I_{814} < 1$) $\wedge$ (S/N(H_{160})>5) $\wedge$ $(\chi^2_{JH_{140}H_{160}}) > 36) \wedge$ $(\chi^2_{K,[3.6],[4.5]} > 2) \wedge (P_{\text{pre}}(z > 8) > 0.5) \wedge (P_{\text{post}}(z > 8) > 0.9)$	$(P(z > 8) > 0.9) \wedge (8.4 < z_{\text{phot}} < 9.5)$
10	idem	$(P(z > 8) > 0.9) \wedge (9.5 < z_{\text{phot}} < 11)$
	CANDELS-EGS	
9	$(J_{125} - H_{160} > 0.5) \wedge (H_{160} - [3.6] < 1.4) \wedge (\text{S/N in both } V_{606} \text{ and } I_{814} < 2) \wedge$ (rms S/N in V_{606} and $I_{814} < 1$) $\wedge$ (S/N(H_{160})>5) $\wedge$ $(\chi_{JH_{140}H_{160}}) > 6) \wedge$ $(\chi^2_{K,[3.6],[4.5]} > 2) \wedge (P_{\text{post}}(z > 8) > 0.9)$	$(P(z > 8) > 0.9) \wedge (8.4 < z_{\text{phot}} < 9.5)$
10	idem	$(P(z > 8) > 0.9) \wedge (9.5 < z_{\text{phot}} < 11)$
	CANDELS-GOODS-North + CANDELS-GOODS-South + ERS	
9	((Y-dropout) criterion from Bouwens+2015) $\vee$ $(J_{125} - H_{160} > 0.5)) \wedge (H_{160} - [3.6] < 1.4) \wedge$ (S/N in both V_{606} and $I_{814} < 2$) $\wedge$ $(\chi^2_{B_{435}V_{606}i_{775}I_{814}z_{850}} < 4) \wedge$ $(P(z > 8) > 0.8) \wedge (8.4 < z_{\text{phot}} < 9.5)$	
10	((Y-dropout) criterion from Bouwens+2015) $\vee$ $(J_{125} - H_{160} > 0.5)) \wedge (H_{160} - [3.6] < 1.4) \wedge$ (S/N in both V_{606} and $I_{814} < 2$) $\wedge$ $(\chi^2_{B_{435}V_{606}i_{775}I_{814}z_{850}} < 4) \wedge$ $(P(z > 8) > 0.8) \wedge (9.5 < z_{\text{phot}} < 11.0)$	

Note.
[a] Redshift likelihood probability $P(z)$ are computed using our flux meaurements in all photometric bands listed in Table 1. $P_{\text{pre}}(z > 8)$ indicates the probability that a source has a redshift greater than 8 before acquiring any follow-up observations, while $P_{\text{post}}(z > 8)$ indicates the probability that a source has a redshift greater than 8 after obtaining the 1-orbit of follow-up *HST* observations (assuming the follow-up observations yielded a measured flux of 0 ± 12 nJy in the Y_{105}-band filter).

Table 3
$z \sim 9$–10 Candidate Galaxies over the CANDELS UDS, COSMOS, and EGS Program Targeted with Our z9-CANDELS Follow-up Program

ID	R.A.	decl.	$H_{160,AB}$	$z_{\text{phot,pre}}$ [a]	$P_{\text{pre}}(z > 8)$ [a]	$z_{\text{phot,post}}$ [b]	$P_{\text{post}}(z > 8)$ [b]
		$z = 9$–10 Candidates Preselected for Targeted Follow-Up Observations with *HST*					
COS910-0	10:00:43.16	02:25:10.5	26.2 ± 0.1	9.1	0.72	7.8	0.47
COS910-1	10:00:30.34	02:23:01.6	26.4 ± 0.2	9.0	0.95	9.0	0.99
COS910-2	10:00:14.91	02:12:10.8	26.3 ± 0.2	9.3	0.74	9.3	0.37
COS910-3	10:00:27.98	02:11:49.5	25.9 ± 0.1	9.2	0.63	2.3	0.27
UDS910-0	02:17:55.50	−05:11:41.3	26.4 ± 0.2	8.8	0.72	1.7	0.09
UDS910-1	02:17:21.96	−05:08:14.7	26.6 ± 0.2	8.7	0.74	8.6	0.74
EGS910-0	14:20:23.47	53:01:30.5	26.2 ± 0.1	9.1	0.67	9.1	0.92
EGS910-1	14:20:21.54	52:57:58.4	26.6 ± 0.1	8.9	0.19[d]	0.4	0.02
EGS910-2	14:20:44.31	52:58:54.4	26.7 ± 0.2	9.6	0.69	9.6	0.71
EGS910-3	14:19:45.28	52:54:42.5	26.4 ± 0.2	8.9	0.64	9.0	0.97
EGS910-4	14:19:23.59	52:49:23.4	26.2 ± 0.2	9.2	0.10[d]	1.0	0.02
EGS910-5	14:19:11.08	52:46:25.7	25.8 ± 0.1	9.2	0.28	1.8	0.11
		$z \sim 9$–10 Galaxy Candidates Targeted at No Additional Cost (Not Preselected)[c]					
EGS910-6	14:19:13.84	52:50:44.7	26.6 ± 0.2	9.3	0.40	7.0	0.00
EGS910-7	14:20:23.72	53:01:38.3	26.0 ± 0.1	...	...	2.4	0.18

Notes.
[a] Best-fit $z > 4$ redshift and integrated $z > 8$ likelihood for source derived from our *HST*+*Spitzer*/IRAC+ground-based photometry (Table 1) before obtaining observations from our z9-CANDELS follow-up program.
[b] Best-fit redshift and integrated $z > 8$ likelihood for source derived from our *HST*+*Spitzer*/IRAC+ground-based photometry (Table 1) after obtaining observations from our z9-CANDELS follow-up program.
[c] These sources could be fit within the same WFC3/IR tiles as our primary targets, and hence required no additional *HST* time to investigate.
[d] Over the CANDELS EGS field, we selected sources which, if they showed a null detection in the Y_{105} band in a 1-orbit integration, could be confirmed with >90% probability to lie at $z > 8$. While these two sources initially only showed a modest probability for being at $z > 8$, their SEDs were nevertheless consistent with lying at $z > 8$ (particularly if a null detection at 1.05 μm could be confirmed).

The most promising $z \sim 9$–10 candidates we identified over the CANDELS-EGS field were EGS910-0, EGS910-2, and EGS910-3. All three sources show evidence for a sharp break break at 1.2 μm as well as a blue spectral slope redward of the break. The other candidates also show evidence for a strong spectral break at 1.2 μm and a blue spectral slope redward of the break, but also show possible flux in ~1–2 passbands blueward of the break. Until observations from our
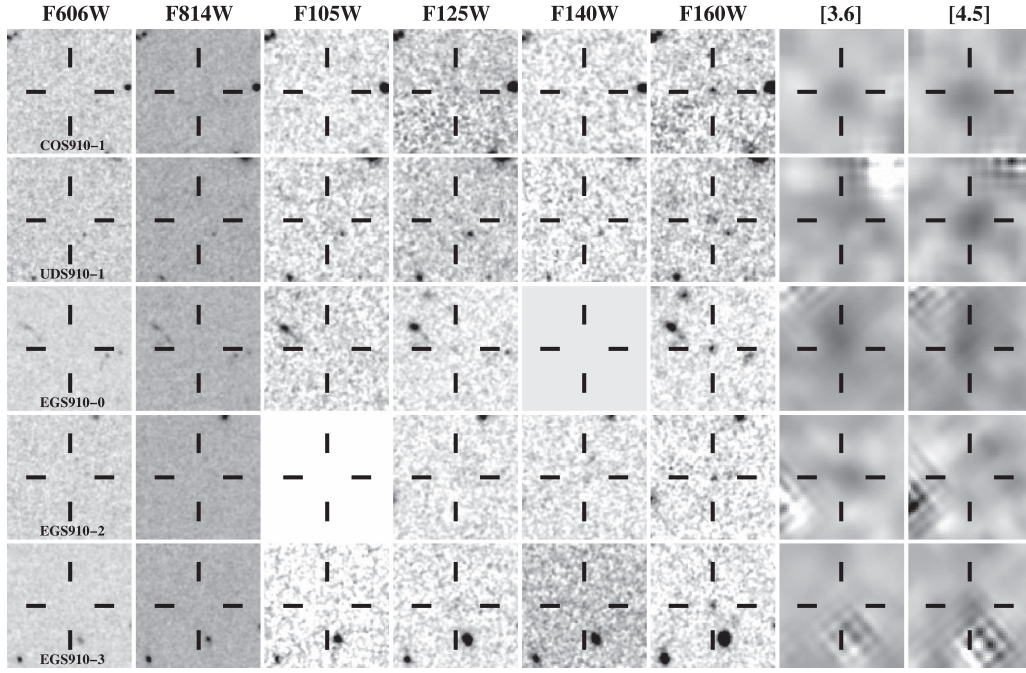
Figure 3. *HST* + *Spitzer*/IRAC images for 5 candidate $z \sim 9$–10 galaxies which were confirmed as probable $z \geqslant 9$ galaxies (or partially confirmed in the case of EGS910-2) using *HST* follow-up observations with our z9-CANDELS program. Fits to the SEDs of these sources and the estimated redshift likelihood distributions are presented in Figure 4.
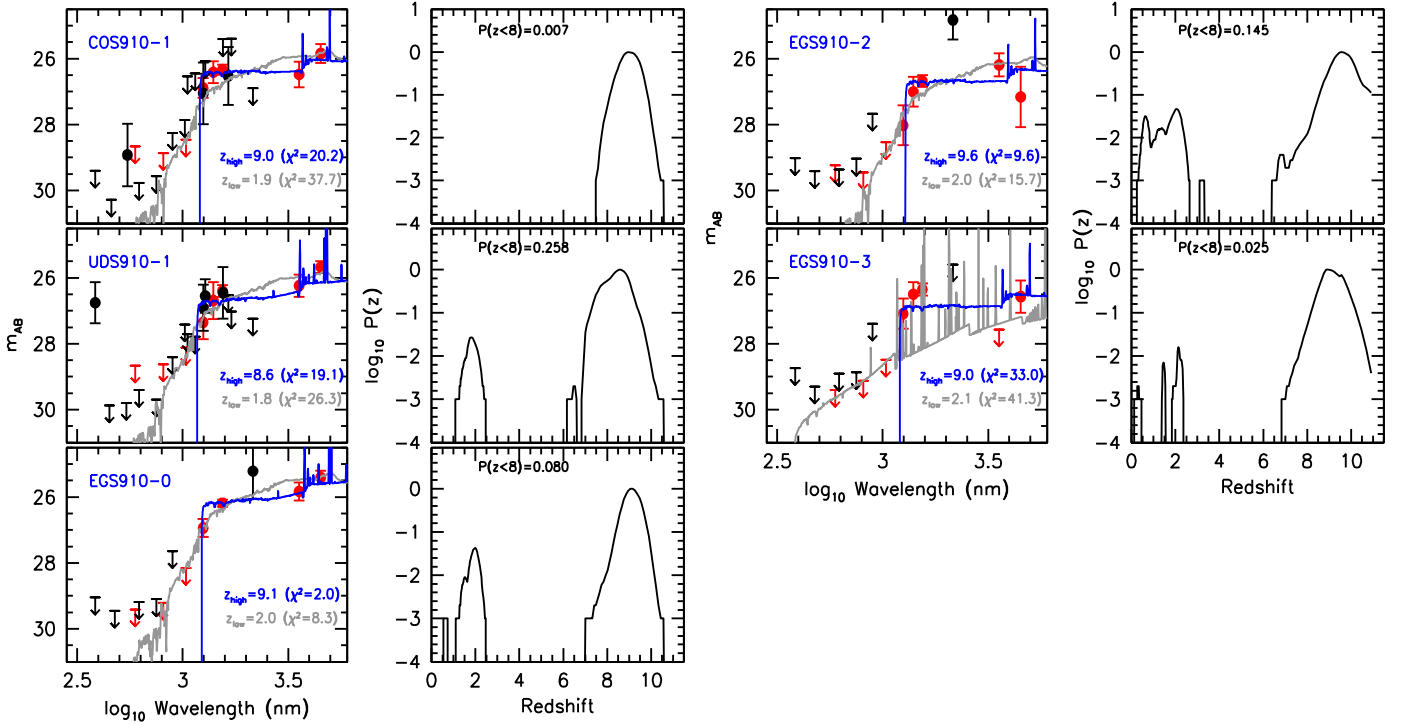
Figure 4. (Left) Best-fit SED models to the observed *HST*+*Spitzer*/IRAC+ground-based photometry of five candidate $z \sim 9$–10 galaxies (COS910-0, UDS910-0, EGS910-0, EGS910-2, EGS910-3) that have been photometrically confirmed (or partially confirmed in the case of UDS910-1 and EGS910-2) by observations from the z9-CANDELS follow-up program. Red solid circles, 1σ error bars, and 1σ limits are from the *HST* or *Spitzer*/IRAC observations, while the black solid circles, 1σ error bars, and 1σ limits are from the ground-based observations. The solid blue line shows the best-fitting SED for a $z > 6$ galaxy, while the gray line shows the best-fitting SED for a $z < 6$ galaxy. (Right) Redshift likelihood distribution for these $z \sim 9$–10 candidates incorporating both our follow-up observations and the *HST*+*Spitzer*/IRAC+ground-based observations that were used in the preselection (solid lines).

z9-CANDELS follow-up program became available on these candidates, it was not possible to determine whether they were more likely to correspond to bona fide $z \sim 9$–10 galaxies or $z \sim 1$–3 interlopers.

4. NATURE OF THE TARGETED $z \sim 9$–10 CANDIDATES

HST observations are now available over all 12 candidate $z \sim 9$–10 galaxies targeted by our z9-CANDELS program. These

Table 4
Photometrically Confirmed $z \sim 9$–10 Galaxies over the CANDELS Fields

ID	R.A.	decl.	$H_{160,AB}$	z_{phot}[a]	$P(z > 8)$	References
			$z \sim 9$ Sample			
Two-part Search Strategy (Preselection + Follow-up: Sections 3, 4):						
COS910-1	10:00:30.34	02:23:01.6	26.4 ± 0.2	$9.0^{+0.4}_{-0.5}$	0.99	
EGS910-0	14:20:23.47	53:01:30.5	26.2 ± 0.1	$9.1^{+0.3}_{-0.4}$	0.92	
EGS910-3	14:19:45.28	52:54:42.5	26.4 ± 0.2	$9.0^{+0.5}_{-0.7}$	0.97	
UDS910-1[b]	02:17:21.96	-05:08:14.7	26.6 ± 0.2	$8.6^{+0.6}_{-0.5}$	0.74	
Direct Search Strategy for $z \geqslant 8.4$ Galaxies (Section 5):						
GS-z9-1	03:32:32.05	-27:50:41.7	26.6 ± 0.2	9.3 ± 0.5	0.9992	(1), (2)
GS-z9-2	03:32:37.79	-27:42:34.4	26.9	$8.9^{+0.3}_{-0.3}$	0.83	(2)
GS-z9-3	03:32:34.99	-27:49:21.6	26.9	$8.8^{+0.3}_{-0.3}$	0.95	(2), (3)
GS-z9-4	03:33:07.58	-27:50:55.0	26.8	$8.4^{+0.2}_{-0.3}$	0.97	(2), (3)
GS-z9-5	03:32:39.96	-27:42:01.9	26.4	$8.7^{+0.8}_{-0.7}$	0.55	(2)
GN-z9-1	12:36:52.25	62:18:42.4	26.6 ± 0.1	9.2 ± 0.3	>0.9999	(1), (2)
			$z \sim 10$ Sample			
Two-part Search Strategy (Preselection + Follow-up: Sections 3, 4):						
EGS910-2[b]	14:20:44.31	52:58:54.4	26.7 ± 0.2	$9.6^{+0.5}_{-0.5}$	0.71	
Direct Search Strategy for $z \geqslant 8.4$ Galaxies (Section 5):						
GN-z10-1[c]	12:36:25.46	62:14:31.4	26.0 ± 0.1	11.1 ± 0.1	>0.9999	(1), (2), (4), (5)
GN-z10-2	12:37:22.74	62:14:22.4	26.8 ± 0.1	9.9 ± 0.3	0.9994	(1), (2)
GN-z10-3	12:36:04.09	62:14:29.6	26.8 ± 0.2	9.5 ± 0.4	0.9981	(1), (2)
GS-z10-1	03:32:26.97	-27:46:28.3	26.9 ± 0.2	9.9 ± 0.5	0.9988	(1), (2)

Notes.

[a] 1σ uncertainties are computed based on the $z > 4$ likelihood distributions.

[b] This candidate could only be partially confirmed, given the limited orbit allocation to our *HST* program.

[c] This source is now spectroscopically confirmed to lie at $z = 11.1$ (Oesch et al. 2016), but broadly lies within our $z \sim 10$ selection window.

References. (1) Oesch et al. (2014), (2) Bouwens et al. (2015), (3) McLure et al. (2013), (4) Oesch et al. (2016), (5) Bouwens et al. (2010).

observations allow us to make a fairly definitive assessment of the nature of these candidate $z \sim 9$–10 galaxies based on the flux we measure for these candidates at 1.05 μm. One orbit of Y_{105}-band observations has already been obtained for eight candidates targeted by our program COS910-0, COS910-1, COS910-3, UDS910-0, UDS910-1, EGS910-0, EGS910-1, EGS910-3, and EGS910-4. Slightly shallower observations (i.e., 1/3 and 2/3 of an orbit) in the Y_{105} band were acquired for the candidates EGS910-5 and COS910-2 due to the greater brightness of the former candidate and the utility of an additional 1/3 orbit JH_{140}-band observations to investigate the nature of the potential $z \sim 10$ candidate galaxies EGS910-2 and COS910-3.

Y_{105}-band images for these candidates are presented in either Figure 3 or Figure 12 from Appendix B, in conjunction with images of these candidates at other wavelengths. Figure 4 and Figure 13 from Appendix B show the observed SEDs for the targetted $z \sim 9$–10 candidates in the CANDELS program.

The present observations photometrically confirm 5 of the first 12 $z \sim 9$–10 candidates targeted by our program. Two of these five confirmations are only partial confirmations (EGS910-2 and UDS910-1: more observations are needed for these candidates to be >90% secure). Detailed remarks on the confirmed $z \sim 9$–10 candidates can be found here.

COS910-1: COS910-1 is not detected ($<1\sigma$) in the Y_{105}-band follow-up observations at 1.05 μm. A detailed fit to its SED suggests that it is actually a star-forming galaxy at $z = 9.1$, with <0.7% probability of it corresponding to a $z < 8$ galaxy.

UDS910-1: UDS910-1 is not detected at ($<1\sigma$) in the Y_{105}-band follow-up observations we obtained at 1.05 μm. Rederiving the redshift likelihood distribution using the new flux information in the Y_{105} band, we compute a best-fit photometric redshift of 8.6 with 4% and 24% probabilities of corresponding to a $z < 7$ and $z < 8$ source, respectively.

EGS910-0: EGS910-0 is not detected ($<1\sigma$) in the Y_{105}-band follow-up observations at 1.05 μm. Rederiving the redshift likelihood distribution using the new flux information in the Y_{105} band, we compute a best-fit photometric redshift of 9.1 with only a 4% probability of corresponding to a $z < 8$ source.

EGS910-2: Follow-up of EGS910-2 in the JH_{140} band shows a clear 2.6σ detection of the source which is in excellent agreement with the expected flux given a model redshift of $z \sim 9.6$ for the source. Nevertheless, the source is sufficiently faint that the redshift likelihood distribution shows a 29% likelihood of the source being at $z < 8$. Deeper follow-up observations at 1.05 μm will be required to rule out the $z < 8$ solution.

EGS910-3: EGS910-3 shows no detection ($<1\sigma$) in the Y_{105}-band follow-up observations we obtained at 1.05 μm. Rederiving the redshift likelihood distribution using the new flux information in the Y_{105} band, we compute a best-fit photometric redshift of 9.0 with a 3% probability of corresponding to a $z < 8$ source.

The three confirmed $z \gtrsim 8.4$ candidates—and two partially confirmed candidates—from our z9-CANDELS program are compiled for convenience in Table 4. We will also include in this table some additional candidates we identify in Section 5

(also as identified by Oesch et al. 2014 and Bouwens et al. 2015).

Our overall confirmation rate is 42% (5/12) for sources preselected by our criteria. We achieve an even higher 56% success rate targeting those sources from our selection which are high-probability (>50%) $z > 8$ galaxies before our follow-up observations. While imperfect, this program is very efficient, supplementing some 270 orbits of *HST* time and hundreds of hours of *Spitzer* time with only 11 orbits of additional *HST* time. By contrast, the CANDELS + ERS programs over the GOODS-North + South cost some $\sim$500 orbits, and we identified only 9 candidates in those data, or 0.02 $z \sim$ 9–10 candidates per invested orbit.

Detailed remarks on the $z \sim$ 9–10 candidate galaxies that were not confirmed by our follow-up program are included in Appendix A.

5. COMPLETING THE CENSUS OF CANDIDATE $z \sim 9$ GALAXIES OVER THE CANDELS GOODS-NORTH, GOODS-SOUTH, AND ERS FIELDS

We can obtain the best constraints on the volume density of bright $z \sim$ 9–10 galaxy candidates by not simply considering a search over the CANDELS UDS, COSMOS, and EGS fields as we did in the previous sections, but also considering a search for similar sources over the GOODS-North and GOODS-South fields.

5.1. Criteria for Identifying $z \sim$ 8.5–9.0 Galaxies

The purpose of the present section is to obtain a complete census of the bright $z \sim$ 8.5–11 galaxy candidates over the CANDELS GOODS-North+GOODS-South + ERS fields.

In Oesch et al. (2014) and Bouwens et al. (2015), we had already conducted a significant search for galaxies in this redshift range by looking for sources with red $J_{125} - H_{160} > 0.5$ colors and blue $H_{160} - [3.6] < 1.4$ colors. However, such a selection is only sensitive to galaxies with redshifts $z \gtrsim 9$ and can suffer significant incompleteness at $z < 9$.

Here, we extend the search from Oesch et al. (2014) and Bouwens et al. (2015) to also consider sources with redshifts $z \gtrsim 8.4$. We select these sources by considering all those sources which satisfy the $z \sim 8$ color–color criteria of Bouwens et al. (2015), deriving photometric redshifts for all such sources using the EAZY photometric redshift code (Brammer et al. 2008) and including those sources where the most likely redshift is greater than 8.4.

The photometry we consider in deriving the redshift likelihood contours are the Bouwens et al. (2015) reductions of the *HST* $B_{435}V_{606}i_{775}I_{814}z_{850}Y_{098}Y_{105}J_{125}JH_{140}H_{160}$ data, the Labbé et al. (2015) reductions of essentially all *Spitzer*/IRAC observations over the GOODS-North and South fields, and the Bouwens et al. (2015) reductions of the HUGS HAWK-I K_s-band observations.

Briefly, the Bouwens et al. (2015) selection criteria for identifying $z \sim 8$ sources is

$$(Y_{105} - J_{125} > 0.45) \wedge (J_{125} - H_{160} < 0.5) \wedge$$
$$(Y_{105} - J_{125} > 0.75(J_{125} - H_{160}) + 0.525)$$

for sources over the CANDELS GOODS-North + GOODS-South fields and

$$(Y_{098} - J_{125} > 1.3) \wedge (J_{125} - H_{160} < 0.5) \wedge$$
$$(Y_{098} - J_{125} > 0.75(J_{125} - H_{160}) + 1.3)$$

for sources over the $\sim$40 arcmin^2 ERS field. Sources are required to be detected at 6σ in a χ^2 stack of the H_{160}-band or $JH_{140} + H_{160}$ band observations redward of the break (in a fixed 0.″36-diameter aperture).

To ensure that contamination is kept to a minimum, an optical "χ^2" is computed for each candidate source (Bouwens et al. 2011b) based on the flux in the $B_{435}V_{606}i_{775}I_{814}z_{850}$-band observations. χ^2_{opt} is taken to equal $\Sigma_i SGN(f_i)(f_i/\sigma_i)^2$, where f_i is the flux in band i in a consistent aperture, σ_i is the uncertainty in this flux, and $SGN(f_i)$ is equal to 1 if $f_i > 0$ and -1 if $f_i < 0$. Any candidate with a measured χ_{opt} in excess of 4 is excluded from our selections.

We only search for $z \gtrsim 8.4$ sources over the GOODS-North and GOODS-South fields brightward of $H_{160,AB} = 27$ mag to ensure that we have strong constraints on the nature of the selected sources to the limit of our search. The effective depth of our $z \sim$ 9–10 search over the CANDELS-UDS, COSMOS, and EGS fields is also approximately $\sim$27 mag, and so the effective depth of our search is similar across all five CANDELS fields that we use.

5.2. Selection Results

Using the selection criteria from the previous section, we identify three high-probability (>90% confidence) and one moderate probability ($\sim$50% confidence) $z \sim$ 8.4–9.0 galaxies over the ERS, CANDELS GOODS-South, and CANDELS GOODS-South fields.

The H_{160}-band magnitudes of the $z \sim$ 8.4–9.0 galaxies we have selected range from 26.4 and 26.9, similar to those found for our $z \sim$ 9–10 sample over the CANDELS-UDS, COSMOS, and EGS fields. We have included the four new $z \sim$ 8.4–9.0 candidates in Table 4 along with other high-probability $z \sim$ 8.4–11 candidates identified here. Fits to the observed SEDs for our new $z \sim$ 8.4–9.0 candidates over these fields are shown in Figure 5. Postage stamp images of the candidates are provided in Figure 6.

5.3. Criteria for Identifying $z \gtrsim$ 9.0 Galaxies

As performed by Oesch et al. (2014) and Bouwens et al. (2015), we also include sources with $J_{125} - H_{160} > 0.5$, $H_{160} - [3.6] < 1.4$ colors. Our selection criteria for identifying these sources are essentially identical to those used by Bouwens et al. (2015: see also Oesch et al. 2014), except we use a $J_{125} - H_{160} > 0.5$ color criterion.

We identify the exact same set of sources identified by Oesch et al. (2014) using the above criteria. A compilation of these sources and other $z \sim$ 8.4–9.0 sources identified over the CANDELS GOODS-North, GOODS-South, and ERS fields is provided in Table 4.

6. IMPACT OF GRAVITATIONAL LENSING FROM FOREGROUND GALAXIES ON THESE RESULTS

From previous work (Wyithe et al. 2011; Barone-Nugent et al. 2015; Fialkov & Loeb 2015; Mason et al. 2015), it is well known that gravitational lensing from foreground galaxies can
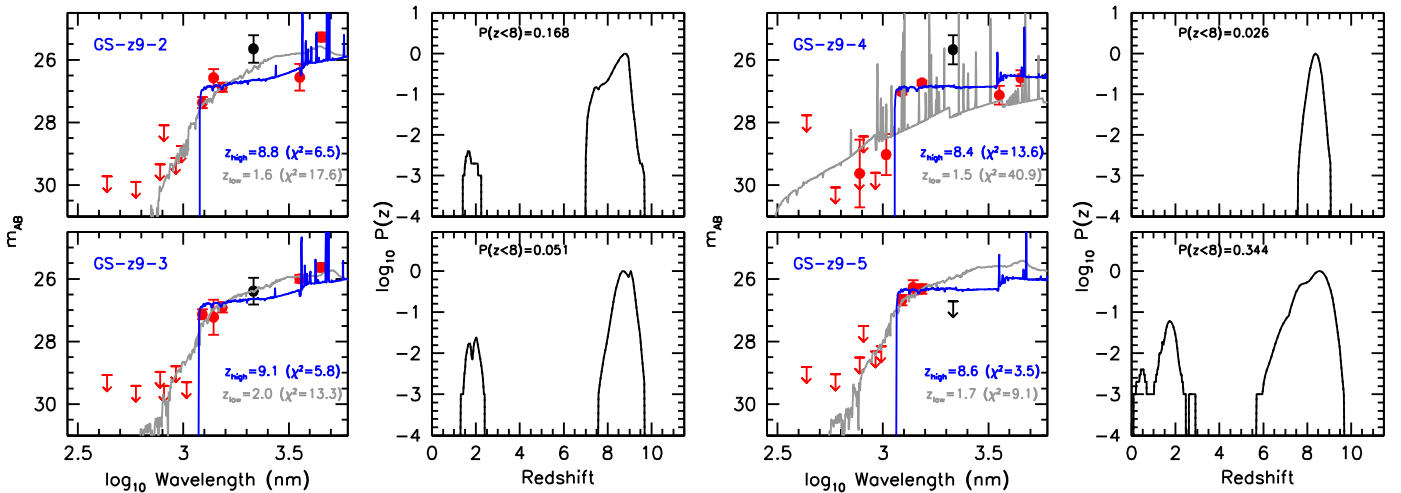
Figure 5. (Left) Best-fit SED models to the observed *HST*+*Spitzer*/IRAC+ground-based photometry of three candidate $z \sim 9$ galaxies (GS-z9-2, GS-z9-3, GS-z9-4) that satisfied our criteria for selection. This figure also includes another candidate $z \sim 9$ galaxy (GS-z9-5) whose nature is sufficiently uncertain that we will treat it as a half candidate for the purposes of deriving the LF (Section 7.1). These sources were identified in a separate search over the extended GOODS-South area (ERS, CANDELS GOODS-South, HUDF09-1, HUDF09-2: see Section 5.1). The points and lines are otherwise as in Figure 4. (Right) Redshift likelihood distribution for these $z \sim 9$ candidates (solid lines).

have a particularly significant effect in enhancing the surface density of bright $z \gtrsim 6$ galaxies on the sky. This is especially true for the brightest sources due to the intrinsic rarity and the large path length available for lensing by foreground sources.

Given this phenomenon, it has become increasingly common for researchers searching for the brightest $z \sim 6$–10 galaxies to look for possible evidence of lensing amplification (Bowler et al. 2014, 2015; Oesch et al. 2014; Zitrin et al. 2015; Roberts-Borsani et al. 2016). While there are a number of cases where such magnification boosts may be present (e.g., Barone-Nugent et al. 2015; Roberts-Borsani et al. 2016), the fraction of lensed sources among bright samples still does not appear to be particularly high (Bowler et al. 2015).

As in the above work, we explicitly check our compilation of bright $z \sim 9$–10 galaxy candidates from these fields for evidence of gravitational lensing. For convenience, we use the Skelton et al. (2014) catalogs providing radii and stellar mass estimates for all sources over the CANDELS areas that we have searched. The Skelton et al. (2014) catalogs use the diverse multi-wavelength data over the CANDELS fields, including *HST* optical, near-infrared, *Spitzer*/IRAC, and ground-based observations, to provide flux measurements of a wide wavelength range, and then use these flux measurements to estimate the redshifts and stellar masses.

As in Roberts-Borsani et al. (2016), we model galaxies in our bright $z \sim 9$–10 sample as singular isothermal spheres and use the measured half-light radius and inferred stellar mass to derive velocity dispersion estimates for individual galaxies in these samples. We found only two examples of galaxies whose measured fluxes appear likely to be slightly boosted (>0.1 mag) by lensing amplification.

EGS910-3: There is a foreground galaxy at $z \sim 1.9$ with an estimated stellar mass of a $10^{10.32}$-$M_\odot$ that lies within 1.9 arcsec of this source. Based on the velocity dispersion we estimate for this source, $\sim$220 km s^{-1}, we compute a magnification boost of 0.25 mag for this source.

GN-z10-2: This source is estimated to be boosted by 0.11 mag by a $10^{10.64}$ $M_\odot$ galaxy with a spectroscopic redshift of $z = 1.02$ (Barger et al. 2008) that lies within 4″0 of the targeted

source. This source was previously flagged by Oesch et al. (2014) as being slightly lensed.

7. IMPLICATIONS OF OUR SEARCH RESULTS

7.1. Constraints on the UV LFs at $z = 9$ and $z = 10$

In this section, we use the combined sample of $z \sim 9$–10 candidates over the CANDELS-UDS, CANDELS-COSMOS, and CANDELS-EGS fields and similar $z \sim 9$–10 candidates over the CANDELS GOODS-North and GOODS-South fields (Section 5) to quantify the UV LFs at $z \sim 9$ and $z \sim 10$. Table 4 provides a compilation of the relevant sources for our determination of the LF.

As in our recent paper on the $z \sim 4$–10 LFs, we use the results from these simulations to derive the selection volumes needed to relate the UV LF function $\phi(M)$ to the observed surface density of sources on the sky. Formally, we write the UV LF in stepwise format ϕ_j as $\Sigma \phi_j W(M - M_j)$, where j is an index running over the magnitude bins, where M_j corresponds to the absolute magnitude at the center of each bin, where

$$W(x) = \begin{array}{ll} 0, & x < -0.4 \\ 1, & -0.4 < x < 0.4 \\ 0, & x > 0.4, \end{array} \qquad (1)$$

and where x gives the position within a magnitude bin. We take the width of the magnitude bins to be 0.8 mag (e.g., versus the 0.5 mag used by Bouwens et al. 2015), given the limited number of bright $z \sim 9$ and $z \sim 10$ galaxies.

We then look for the derived LF ϕ_j that yields the observed surface density of $z \sim 9$ and $z \sim 10$ galaxies on the sky with maximum probability $\mathcal{L}$. As in Bouwens et al. (2015), the likelihood $\mathcal{L}$ is computed as

$$\mathcal{L} = \Pi_{\text{field}} \Pi_i p(m_i), \qquad (2)$$

where the above products run over the different search fields and magnitude interval i used in the LF determinations, and where $p(m_i)$ is the probability of identifying a certain number of sources in magnitude interval i in a given search field.
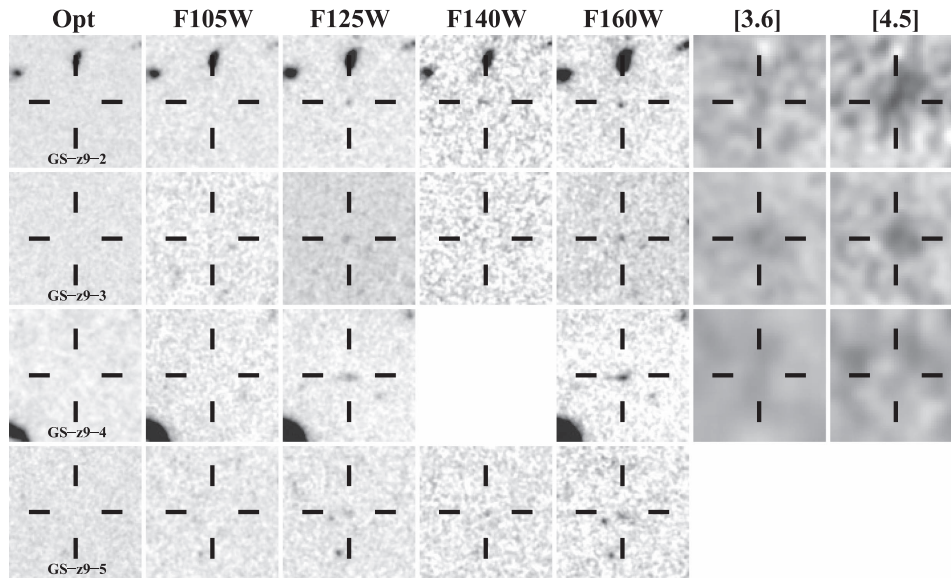
Figure 6. *HST* + *Spitzer*/IRAC images (6″ × 6″) of three candidate $z \sim 9$ galaxies (GS-z9-2, GS-z9-3, GS-z9-4) that satisfied our criteria for selection and another candidate $z \sim 9$ galaxy (GS-z9-5) that did not satisfy these criteria (but which we will treat as half of a $z \sim 9$ galaxy for the purposes of deriving the LFs). We have identified these candidates in a separate search over the extended GOODS-South area (ERS, CANDELS GOODS-South, HUDF09-1, HUDF09-2: see Section 5.1).

For simplicity (and given the small numbers in each of our samples: see the discussion in Section 4 of Bouwens et al. 2008), we ignore field-to-field variance in deriving the LF results and compute the likelihood that our survey fields show a certain number of sources assuming Poissonian statistics. We therefore compute $p(m_i)$ as follows:

$$p(m_i) = e^{-N_{\mathrm{exp},i}} \frac{(N_{\mathrm{exp},i})^{N_{\mathrm{obs},i,j}}}{(N_{\mathrm{obs},i,j})!}, \qquad (3)$$

where $N_{\mathrm{obs},i}$ is the observed number of sources in search field and magnitude interval i, and $N_{\mathrm{exp},i}$ is the expected number of sources in a search field and magnitude interval i. The expected number of sources in a search field $N_{\mathrm{expected},i}$ is computed as

$$N_{\mathrm{expected},i} = \Sigma_j \phi_j V_{i,j}, \qquad (4)$$

where $V_{i,j}$ is the effective volume over which one could expect to find a source of absolute magnitude j in the observed magnitude interval i.

The selection volumes $V_{i,j}$ are estimated using an almost identical procedure to that in Bouwens et al. (2015). Specifically, we constructed catalogs with mock sources spanning the entire redshift range $z \sim 7.5$ to $z \sim 12$. To ensure that sources had reasonable sizes and morphologies, we randomly selected similar luminosity $z \sim 4$ galaxies from the Hubble Ultra Deep Field (Beckwith et al. 2006; Illingworth et al. 2013) to use as a template for modeling the two-dimensional pixel-by-pixel profiles of individual sources. The sizes of the model sources were assumed to scale with redshift as $(1 + z)^{-1.2}$ to match the size scaling observed for sources with fixed luminosity from $z \sim 10$ to $z \sim 2$ (Oesch et al. 2010; Ono et al. 2013; Holwerda et al. 2015; Bouwens et al. 2015; Kawamata et al. 2015; Shibuya et al. 2015). The UV-continuum slopes of sources were assumed to have a mean value of -1.8, which is consistent with that measured at high luminosities at $z \sim 5$–8 (Bouwens et al. 2012; Finkelstein et al. 2012; Willott et al. 2013; Bouwens 2014; Rogers et al. 2014), with a dispersion of 0.3 (Bouwens et al. 2012; Castellano et al. 2012).

We generate simulated images of each source in all *HST*, ground-based, and *Spitzer*/IRAC wavelength channels. Artificial images of individual sources in the ground-based and *Spitzer*/IRAC channels are produced by convolving the simulated *HST* images with the PSF-matching kernels we derive with MOPHONGO (Labbé et al. 2013). These images are then added to sections of the CANDELS UDS, COSMOS, EGS, GOODS-North, and GOODS-South, and ERS fields, catalogs are constructed, and sources are selected using exactly the same procedures as we apply to the real observations. We include both the criteria used for our preselection and our confirmation criteria (i.e., $P(z > 8) > 0.9$) in computing the selection volume. We implement these criteria in a manner identical to how they are applied to the observations.

For example, to be included in our selection volume estimates, simulated sources are preselected using the criteria we describe in Section 3.2.1 or 3.3.1. For simulated sources within the CANDELS-UDS and CANDELS-COSMOS data sets, this means that their cumulative probability of lying at $z > 8$ must be greater than 50% before the addition of any Y_{105}-band data. In addition, simulated sources (over the CANDELS-UDS/COSMOS/EGS fields) must show a probability $>90\%$ of lying at $z > 8$ after the inclusion of the flux constraint (0 ± 12 nJy: nominally the flux constraint one would obtain for a $z \sim 9$–10 galaxy based on a single orbit of Y_{105}-band observations) and must have a measured $J_{125} - H_{160}$ color >0.5 mag. Our simulation results make it clear how important the preselection can be. While increasing the efficiency of our search results significantly, preselection can also introduce a modest amount of incompleteness into the $z \sim 9$–10 samples we identify from CANDELS, particularly at $z < 9$ (where it is $\sim 40\%$ from the preselection step alone).

In addition to considering the selection of sources from CANDELS-UDS, CANDELS-COSMOS, and CANDELS-UDS fields, we also consider the selection of $z \sim 9$ and $z \sim 10$ galaxies from the CANDELS GOODS-North, CANDELS GOODS-South, and ERS fields.

In computing the number of confirmed $z = 9$–10 sources from our program, we assume all of the sources in Table 4 are
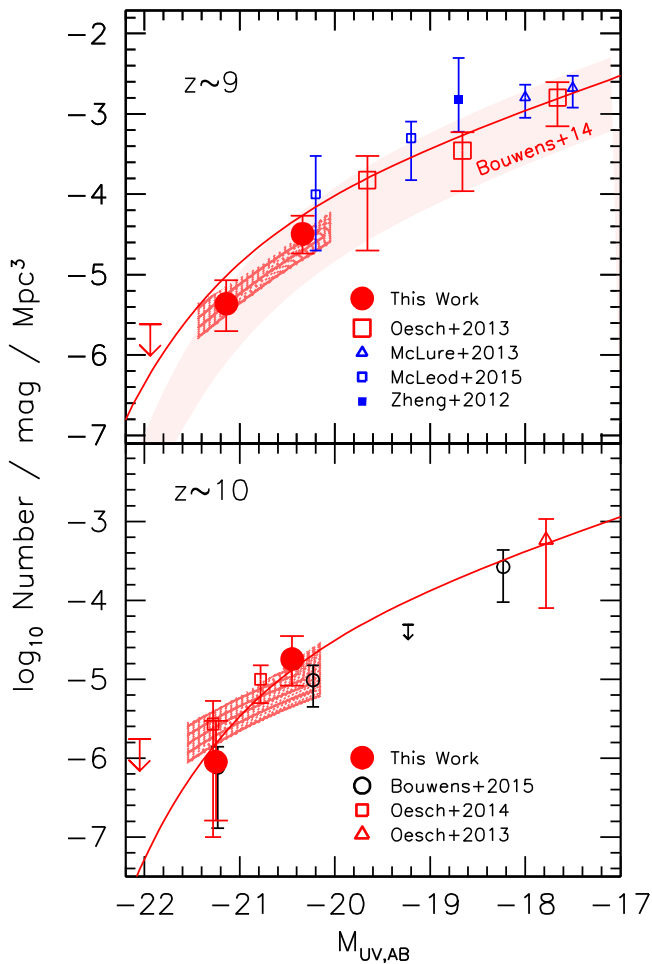
Figure 7. Simple binned determinations of the UV LF for luminous galaxies at $z = 9$ (upper panel) and $z = 10$ (lower panel). 1σ upper limits on the volume density of $z \sim 9$ and $z \sim 10$ galaxies are included at ~ -22 mag. The shaded hatched red region indicates the volume densities (at a given M_{UV}) preferred at 68% confidence by this analysis (see Table 6). To put these constraints on the bright end of the UV LF in context, we also include determinations of the $z \sim 9$ and $z \sim 10$ UV LFs at lower luminosities from Zheng et al. (2012: solid blue square), Oesch et al. (2013: open red square), McLure et al. (2013: open blue triangles), and McLeod et al. (2015: open blue squares). The lightly shaded red region shows the constraints on the $z \sim 9$ LF as derived by Bouwens et al. (2014a) using a search for $z \sim 9$ galaxies over the CLASH program (Postman et al. 2012). The overplotted line shows an extrapolation of the Bouwens et al. (2015) LF results to $z \sim 9$ and $z \sim 10.2$ based on the fitting formula provided in Section 7.1.

Table 5
Binned Determination of the Rest-frame UV LF at $z \sim 9$ and $z \sim 10$

$M_{1600,AB}$[a]	ϕ_k (10^{-3} Mpc^{-3} mag^{-1})
$z \sim 9$ galaxies	
-21.94	<0.0024[b]
-21.14	$0.0044^{+0.0042}_{-0.0024}$
-20.34	$0.0322^{+0.0217}_{-0.0138}$
$z \sim 10$ galaxies	
-22.05	<0.0017[b]
-21.25	$0.0009^{+0.0021}_{-0.0007}$
-20.45	$0.0180^{+0.0174}_{-0.0098}$

Notes.
[a] Derived at a rest-frame wavelength of 1600 Å.
[b] 1σ upper limit.

Table 6
68% Confidence Regions on the Volume Density of Galaxies at $z \sim 9$ and $z \sim 10$ vs. M_{UV}

$M_{1600,AB}$[a]	Volume Density (10^{-3} Mpc^{-3} mag^{-1})	
	Lower Bound[b]	Upper Bound[b]
$z \sim 9$ galaxies		
-21.84	0.0006	0.0024
-21.64	0.0010	0.0032
-21.44	0.0016	0.0044
-21.24	0.0024	0.0060
-21.04	0.0039	0.0084
-20.84	0.0059	0.0120
-20.64	0.0087	0.0174
-20.44	0.0126	0.0262
-20.24	0.0176	0.0402
-20.04	0.0250	0.0621
$z \sim 10$ galaxies		
-21.95	0.0004	0.0018
-21.75	0.0006	0.0022
-21.55	0.0009	0.0028
-21.35	0.0012	0.0036
-21.15	0.0017	0.0048
-20.95	0.0023	0.0066
-20.75	0.0030	0.0093
-20.55	0.0039	0.0135
-20.35	0.0049	0.0200
-20.15	0.0060	0.0299

Notes.
[a] Derived at a rest-frame wavelength of 1600 Å.
[b] 68% Confidence Region.

bona fide $z \sim 9$–10 galaxies and that there is no contamination in our selection. This would appear to be a good assumption, given that the typical $z \sim 9$–10 candidate formally prefers a $z > 8$ solution at 99% likelihood. We do not include EGS910-2 and UDS910-1 in our LF calculation since they do not meet our formal criteria for inclusion (but nevertheless appear to be probable $z \gtrsim 8.5$ galaxies). We suppose that all of the candidates from our follow-up program that were not explicitly confirmed by that program lie at $z < 8.4$ (all but one of these candidates was detected at $\geqslant 2\sigma$ in the follow-up Y_{105}-band observations and are therefore unlikely $z > 8.4$). The $z \sim 9$ candidate GS-z9-5 is modeled as a 0.5 $z \sim 9$ galaxy (i.e., $\sim 50\%$ probability of contamination) given that its computed $P(z > 8)$ was only 0.66 (Figure 5). We ignore the impact of possible lensing amplification on one source in our selection (EGS910-3) given the size of the magnification factor

(0.25 mag) and the fact that source volume and magnification factor trade off in such a way as to have little impact on the derived LF.

Our $z \sim 9$ and $z \sim 10$ LF results are presented in Figure 7 and tabulated in Table 5. In computing the uncertainties on the $z \sim 9$ and $z \sim 10$ UV LFs, we also include the expected large-scale structure uncertainties, using the results from the cosmic variance calculator of Trenti & Stiavelli (2008) and the observed comoving volume density. For context, the earlier LF results of McLure et al. (2013), Oesch et al. (2013, 2014), Bouwens et al. (2014a, 2015), and McLeod et al. (2015) are presented in Figure 7.

Given the limited number of $z \sim 9$–10 candidates in our samples and some arbitrariness in the choice of bin centers (and
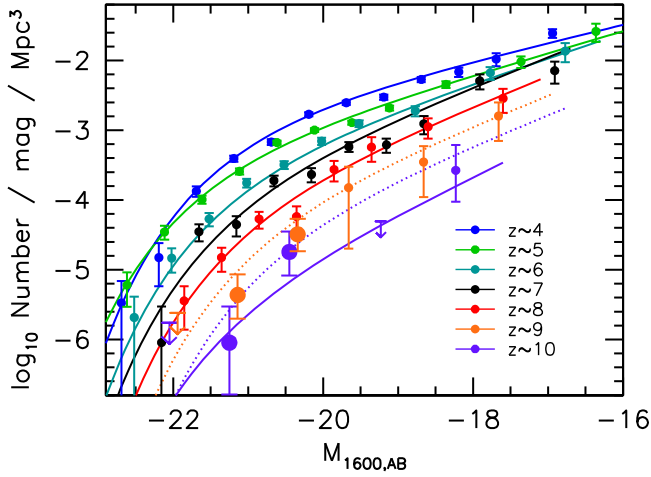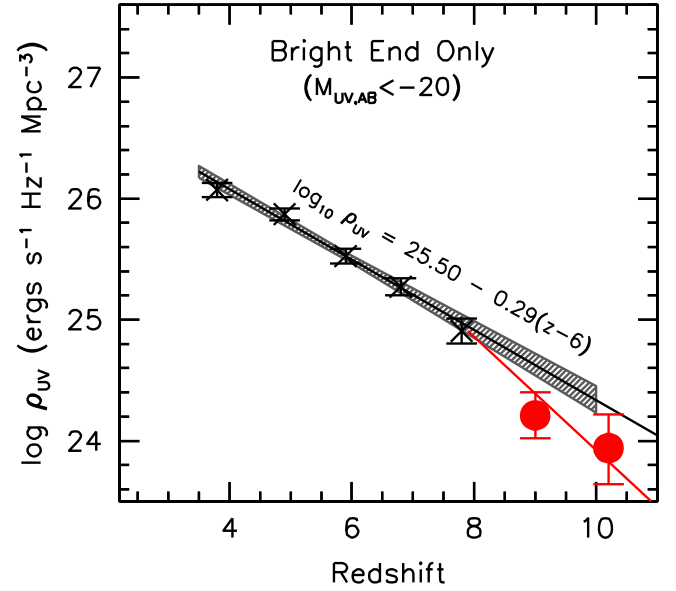
Figure 8. Present determinations of the bright end of the UV LF at $z \sim 9$ and $z \sim 10$ using all five CANDELS fields (orange and dark purple circles, respectively, with 1σ uncertainties). 1σ upper limits are as in Figure 7. For context, we also include fainter determinations of the UV LFs at $z \sim 9$ and $z \sim 10$ from Oesch et al. (2013) and Bouwens et al. (2015: small circles and solid line). The dashed lines indicate extrapolations of the Bouwens et al. (2015) LF relations to $z \sim 9$ and $z \sim 10.2$ (see Section 6.1). The $z \sim 4$, $z \sim 5$, $z \sim 6$, $z \sim 7$, and $z \sim 8$ LF determinations from Bouwens et al. (2015) are also shown.

Figure 9. Present determinations of the UV luminosity density of galaxies at $z \sim 9$ and $z \sim 10$ (solid red circles) brightward of -20 mag using the present search over all 5 CANDELS fields. The black crosses show the luminosity density of galaxies brightward of -20 mag determined by Bouwens et al. (2015) at $z \sim 4$, $z \sim 5$, $z \sim 6$, $z \sim 7$, and $z \sim 8$. The shaded region shows the evolutionary trend to $z > 8$ in the UV luminosity density preferred at 68% confidence. The red line shows the observed evolution in the UV luminosity density beyond $z \sim 8$ and can be approximately represented by $d \log_{10} \rho_{\rm UV}/dz = -0.45 \pm 0.07$ dex. The UV luminosity density we find for luminous $z \sim 9$ and $z \sim 10$ galaxies lies below a simple extrapolation of the evolution from $z \sim 4$ to $z \sim 8$.

width) for our stepwise $z \sim 9$–10 LF results, it is conceivable that our $z \sim 9$–10 LF results could depend on how we bin our sample. We therefore also model the bright end of the LF as a power law (motivated by the results of, e.g., Bowler et al. 2014 and Bouwens et al. 2015). By marginalizing over both the normalization and power-law slope of the model LFs, we derive constraints (68% confidence levels) on the volume density of the $z \sim 9$–10 galaxy candidate for a given $M_{\rm UV}$. These results are presented in Figure 7 and shown in Table 6.

To guide expectations, in Figure 7 we also include the LFs we derive by extrapolating the LF results from Bouwens et al. (2015) to $z \sim 9$ and $z \sim 10.2$ (the mean redshift of our $z \sim 9$ and $z \sim 10$ derived from our selection volume simulations). In deriving a fitting formula from the Bouwens et al. (2015) results, we only consider evolution over the range from $z \sim 8$ to $z \sim 5$ where the UV LF evolves in a relatively smooth manner. This results in the Schechter parameters depending on redshift in the following manner: $M_{\rm UV}^{*} = (-20.97 \pm 0.10) + (0.17 \pm 0.10)(z - 6)$, $\phi^{*} = (0.45_{-0.08}^{+0.10})10^{(-0.21 \pm 0.09)(z-6)}10^{-3}$ Mpc^{-3}, $\alpha = (-1.91 \pm 0.05) + (-0.13 \pm 0.05)(z - 6)$. This fitting formula implies $M^{*} = -20.45$, $\phi^{*} = 0.10 \times 10^{-3}$ Mpc^{-3}, and $\alpha = -2.3$ at $z \sim 9$ and $M^{*} = -20.28$, $\phi^{*} = 0.059 \times 10^{-3}$ Mpc^{-3}, and $\alpha = -2.46$ at $z \sim 10.2$. The best-fit evolutionary scenario from Bowler et al. (2014) is very similar to what we present above (where it was found that $dM^{*}/dz \sim 0.2$).

Relative to these extrapolations of the $z = 4$–8 results to $z > 8$, our present LFs are typically $1.5\times$ lower in the mean, which is consistent with slightly faster evolution at $z > 8$. The results from the above fitting formula are also featured in Figure 8 where we combine the new LF results with previous results from the literature at $z \sim 4$, $z \sim 5$, $z \sim 6$, $z \sim 7$, and $z \sim 8$.

The present estimates of the volume density of particularly bright $z \sim 9$ galaxies are the first available in the literature and have comparable uncertainties to the bright end of the present

LF determinations at $z \sim 10$ (and as derived earlier: Oesch et al. 2014; Bouwens et al. 2015).

7.2. Evolution of the UV Luminosity Density for Luminous Galaxies from $z \sim 10$ to $z \sim 4$

With the present constraints on the volume density of bright galaxies at $z \sim 9$ and $z \sim 10$, we can examine the evolution of the luminosity density of galaxies in the rest-frame UV with cosmic time.

Integrating the light in our binned representation of the bright end of the $z \sim 9$ and $z \sim 10$ LFs to -20 mag (approximately the faint-end limit of the present bright search), we derive a total UV luminosity density $\rho_{\rm UV}$ of $10^{24.21_{-0.19}^{+0.13}}$ erg s^{-1} Hz^{-1} Mpc^{-3} at $z \sim 9$ and $10^{23.94_{-0.28}^{+0.18}}$ erg s^{-1} Hz^{-1} Mpc^{-3} at $z \sim 10$. These inferred luminosity densities are $5_{-2}^{+3}\times$ and $8_{-3}^{+9}\times$ lower, respectively, than those found by Bouwens et al. (2015) at $z \sim 8$.

In Figure 9, we compare the derived luminosity density $\rho_{\rm UV}$ at $z \sim 9$ and $z \sim 10$ with the UV luminosity density derived by Bouwens et al. (2015) from $z \sim 4$ to $z \sim 8$ to the same limiting magnitude. Also shown in this figure is the best-fit evolution (68% confidence intervals) derived for the UV luminosity density based on the $z \sim 4$–8 results. Our new luminosity density results $\rho_{\rm UV}$ at $z \sim 9$ and $z \sim 10$ are $2.6_{-0.9}^{+1.5}\times$ and $2.2_{-1.1}^{+2.0}\times$ lower than the extrapolated luminosity densities at $z \sim 9.0$ and $z \sim 10.2$.

The present results are therefore consistent with a more rapid evolution at $z > 8$ than between $z \sim 8$ and $z \sim 4$, as first noted by Oesch et al. (2012), with a best-fit $d \log_{10} \rho_{\rm UV}/dz$ evolution of -0.45 ± 0.07 versus the -0.29 ± 0.02 evolution observed from $z \sim 8$ to $z \sim 4$. Interestingly, the evolution we derive here

is completely consistent with the $d \log_{10} \rho_{UV}/dz = -0.54^{+0.19}_{-0.36}$ scaling previously derived by Oesch et al. (2012). It is also consistent with the $(1 + z)^{-10.9}$ evolutionary scalings considered in Oesch et al. (2014: see also Oesch et al. 2013).

Other authors (Ishigaki et al. 2015; McLeod et al. 2015; Oesch et al. 2015) have remarked that there is less evidence for faster evolution in the UV luminosity density at $z > 8$ integrated to lower luminosities, particularly when incorporating new results from the full Hubble Frontier Fields program (Lotz et al. 2014; Coe et al. 2015). If the HUDF/XDF is systematically underdense in $z \sim 9$–10 galaxies or if the evolution of the LF proceeds more smoothly for lower-luminosity galaxies, then one might expect such a result. A much more definitive exploration of this issue will be possible if we consider the much larger number of faint sources at $z \sim 9$–10 expected from the full Frontier Fields program (Coe et al. 2015).

8. SUMMARY

In this paper, we provide improved constraints on the volume density of especially luminous ($H_{160,AB} < 27$) $z \sim 9$ galaxies by making use of a search over all 5 CANDELS fields (750 arcmin^2 area in total). We also rederive the bright end of the $z \sim 10$ LF and extend it slightly fainter, taking advantage of the additional search power provided by the S-CANDELS data (Ashby et al. 2015) over the CANDELS-UDS, COSMOS, and EGS fields.

To obtain these constraints, we extend the earlier sample of 6 bright $z \sim 9$ and $z \sim 10$ galaxies identified by Oesch et al. (2015) to make use of the search area over all 5 CANDELS fields, including an additional ~450 arcmin^2 area over the CANDELS-UDS, CANDELS-COSMOS, and CANDELS-EGS fields. We also expand the Oesch et al. (2014) search over the GOODS-South and GOODS-North to obtain a more complete selection of galaxies over the redshift range $z \sim 8.4$–9.0 (see Section 5).

To identify a robust sample of bright $z \sim 9$ and $z \sim 10$ galaxies over this new area, we employed a two-part strategy for selecting sources. To begin, we selected those sources that showed the highest probability of corresponding to $z \sim 9$ and $z \sim 10$ galaxies based on the existing observations. Such identifications were possible given the depth of the *HST* and ground-based imaging observations which placed constraints on both the sharpness of a possible spectral break at 1.2 μm and the spectral slope blueward of the break.

The second step was to obtain deep observations on each of these candidates at 1.05 μm to test the nature of these candidates. These follow-up observations were obtained with the 11-orbit *HST* program z9-CANDELS (Bouwens 2014: GO 13792).

Using the new *HST* observations from the z9-CANDELS program, we find that 5 out of the 12 $z \sim 9$–10 candidates that we followed up with our program appear to be bona fide bright $z \sim 9$–10 galaxies (Figure 4).

Combining our new samples with previous samples of luminous $z \sim 9$–10 candidates over CANDELS GOODS-North and GOODS-South (Oesch et al. 2014), and also including four probable $z \sim 8.4$–9.0 galaxies we identified over the GOODS-S field (finding no additional bright sources over the GOODS-N field), we identify a total sample of 15 bright $z \sim 9$–10 candidates over the five CANDELS fields (Table 4). This is $\gtrsim 2\times$ larger than the sample of luminous $z \sim 9$–10 galaxies we identified earlier in Oesch et al. (2014).

We use these larger samples of $z \sim 9$–10 galaxies to derive improved constraints on the bright end of the $z \sim 9$ and $z \sim 10$ LFs. We achieve these results by simulating both stages in the selection process (for the CANDELS-UDS, COSMOS, and EGS fields)—or a single stage in the case of the CANDELS GOODS-North, GOODS-South, or ERS fields—to arrive at statistically robust conclusions.

As one would expect with any follow-up program of limited size, the z9-CANDELS program is not able to observe all potential $z \sim 9$ and $z \sim 10$ galaxies over the CANDELS-UDS, COSMOS, and EGS fields[11], and therefore likely suffers from moderate incompleteness, particularly for galaxies at $z < 9$, due to our exclusively preselecting follow-up sources with redder $J_{125} - H_{160} > 0.5$ colors than galaxies which exist in this range. Some incompleteness would also result from the detection of spurious flux in the optical bands (~25% effect). Nevertheless, we remark that all such effects are included in our selection volume simulations and our focus on $J_{125} - H_{160} > 0.5$ galaxies means that our search is most complete at $z > 9$.

We would expect these results to be improved, particularly toward fainter magnitudes, if even deeper observations over the CANDELS-UDS, CANDELS-COSMOS, and CANDELS-EGS fields could be obtained. Deeper observations in the F105W band should increase the size of our bright ($H_{160,AB} \lesssim 27$) $z \sim 9$–10 samples over the CANDELS-WIDE fields by improving the completeness of our search results at $z < 9$.[12] Meanwhile, deeper observations in various redder bands (e.g., $JH_{140,AB}$) would allow us to extend these searches to even fainter magnitudes (i.e., to >26.5 mag). We would also expect gains from analysis of the 500-orbit, 500 arcmin^2 BoRG$_{[z910]}$ program (Trenti 2014).

APPENDIX A
POSTAGE STAMPS AND SEDs OF THE TARGETED CANDIDATES

We identified 12 candidate $z = 9$–10 sources over the CANDELS-UDS, CANDELS-COSMOS, and CANDELS-EGS fields that we explicitly targeted for follow-up observations.

Postage stamp images of these 12 candidates are presented in Figure 10. As should be obvious from this figure, all six of the present $z \sim 9$–10 candidates show clear detections in the H_{160} band as well as significant ~2–3σ detections in the J_{125}-band and JH_{140}-band observations (where available), as well as in the S-CANDELS *Spitzer*/IRAC data.

---

[11] Several possible examples of missed $z \sim 9$–10 candidates could include those lower-probability candidates tabulated in Appendix C.

[12] While our selection of $z \sim 9$–10 galaxies is fairly complete at $z > 9$, it suffers greater incompleteness at $z \sim 8.4$–9.0, due to our use of a $J_{125} - H_{160} > 0.5$ criterion in preselecting candidate $z \sim 9$–10 galaxies to follow-up. The addition of Y_{105}-band observations to these fields would allow such sources to be selected much more efficiently.
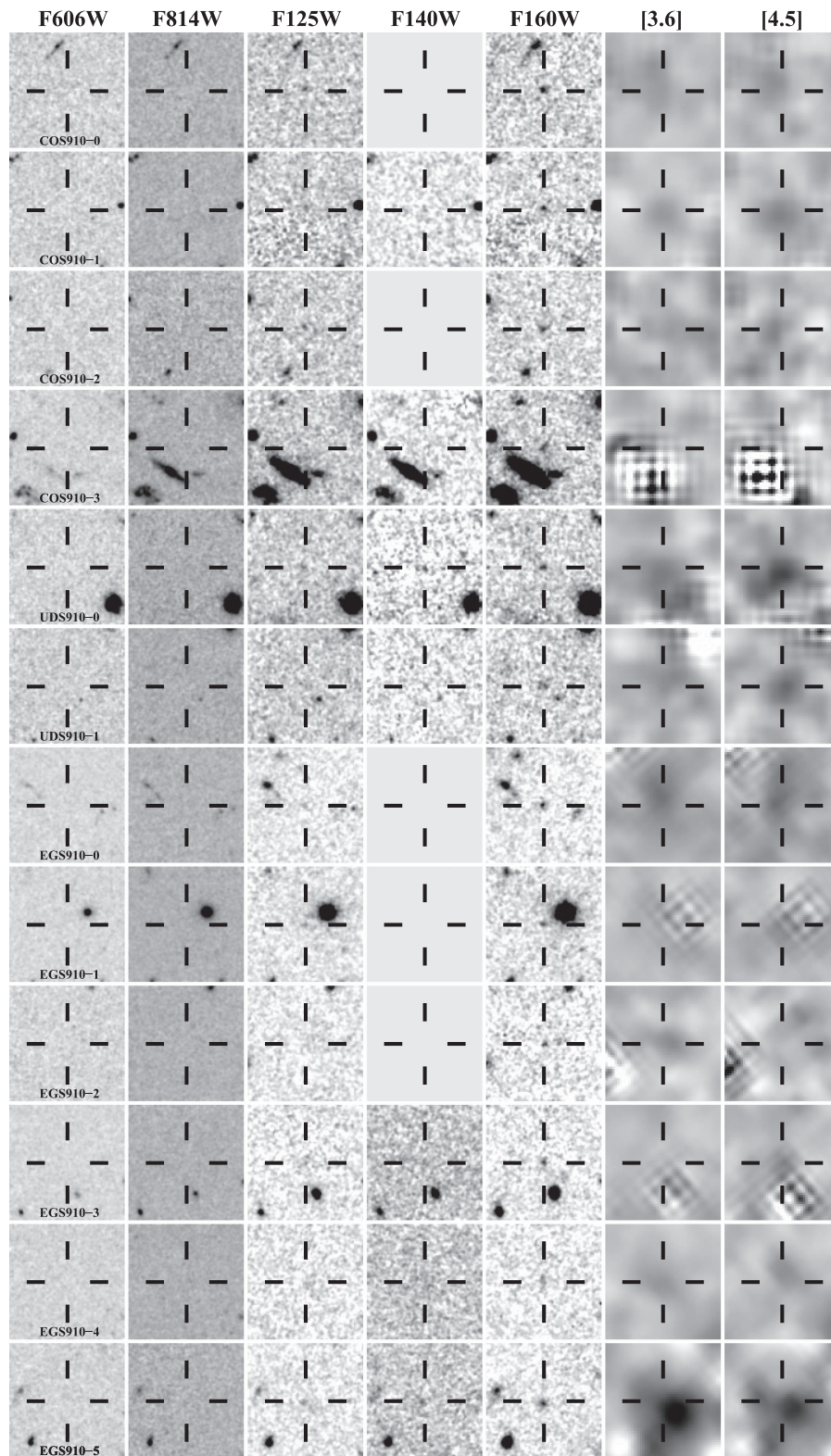
Figure 10. *HST* + *Spitzer*/IRAC images (6″ × 6″) of all preselected candidate $z \sim 9$–10 galaxies over the CANDELS-UDS + CANDELS-COSMOS + CANDELS-EGS fields that were preselected for targeted follow-up with the z9-CANDELS program. The best-fit model flux from neighboring sources has been removed in the *Spitzer*/IRAC images shown here. Our preselected CANDELS-UDS and CANDELS-COSMOS candidates (1) are estimated to show a >50% probability of corresponding to a $z > 8$ galaxy and (2) can be confirmed to lie at $z > 8$ with >90% confidence with the addition of a single orbit of *HST* follow-up observations (assuming a flat redshift prior and the EAZY SED template set). Each of the preselected CANDELS-EGS candidates shown here can be confirmed to be secure at >90% probability with a single orbit of *HST* follow-up observations. Each of these candidates was subject to 1-orbit follow-up observations with our z9-CANDELS program at 1.05 μm.
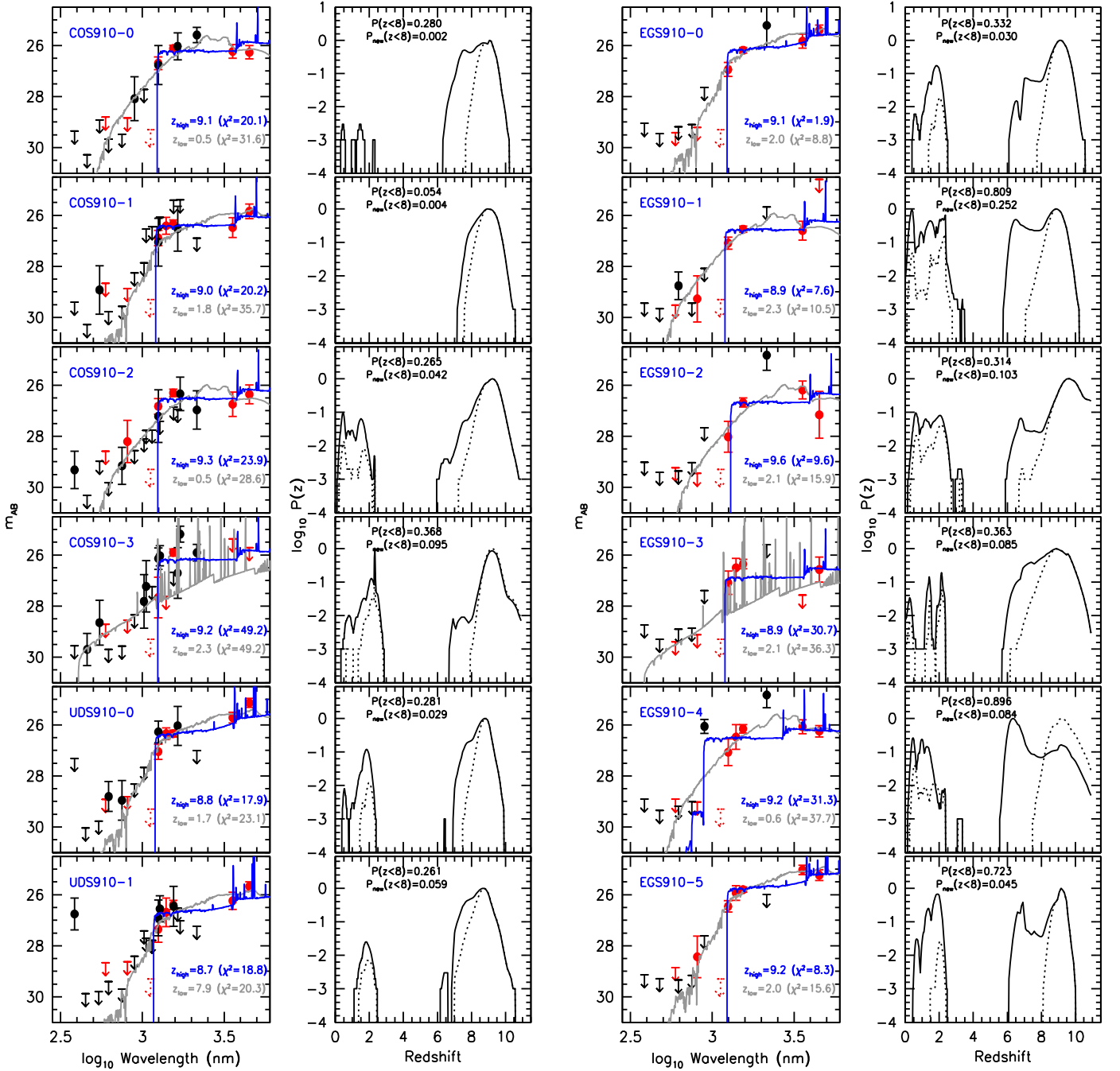
Figure 11. (Leftmost column) Best-fit SED models to the observed *HST*+*Spitzer*/IRAC+ground-based photometry of the preselected candidate $z \sim 9$–10 galaxies we have identified for targeted follow-up with the z9-CANDELS follow-up program. The dotted red upper limits show the approximate constraints we will be able to set on the 1.05 μm fluxes of the candidates, assuming they are at $z \gtrsim 8.4$. The points and lines are otherwise as in Figure 4. (Second leftmost column) Redshift likelihood distribution for the same 12 $z \sim 9$–10 candidates using current observations (solid lines) and also making use of our 1-orbit Y_{105}-band follow-up observations (dotted lines) assuming the sources are at $z \gtrsim 9$. $P(z < 8)$ and $P_{\text{new}}(z < 8)$ indicate the probability that our candidates are at $z < 8$ using the current observations and including our follow-up observations (again assuming they are $z \gtrsim 9$). It should be clear that our z9-CANDELS follow-up observations should significantly improve our confidence in the present set of $z \gtrsim 9$ candidates, increasing it from 72%–95% to 95.8%–99.8%.
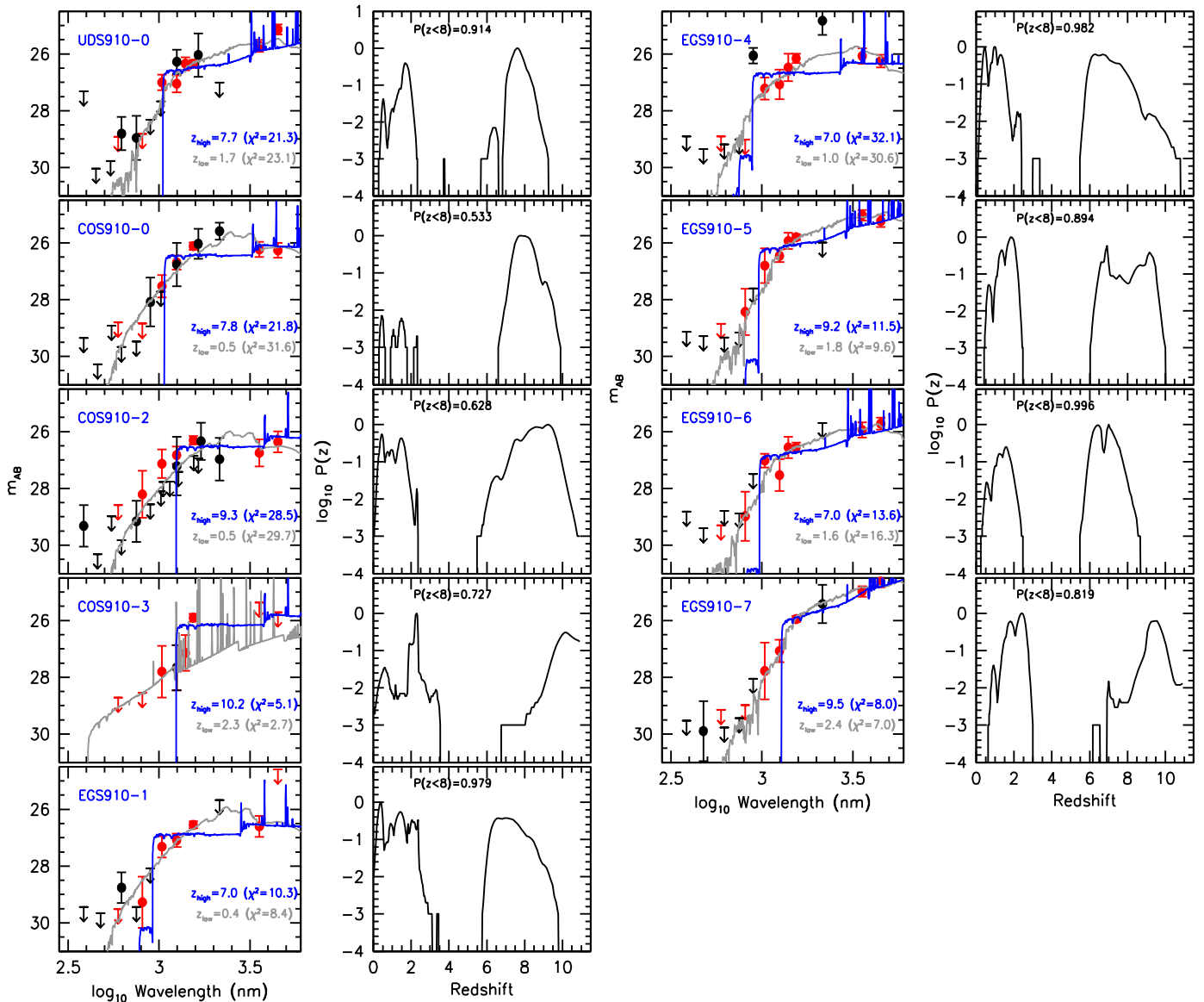
The observed photometry to those candidate sources are presented in Figure 11 along with SED fits to a model $z > 8$ galaxy and a model $z < 3$ galaxy. Also shown in this figure is the redshift likelihood distribution (*solid black line*) based on the photometry we have available for each candidate in the ~20 different wavelength channels (*HST* + *Spitzer*/IRAC + ground-based observations). In addition, this figure presents the redshift likelihood distribution we would expect, assuming

that these candidates are not detected in the single orbit of follow-up Y_{105}-band observations from the z9-CANDELS program.

All 12 candidates show $H_{160} - [3.6]$ colors (see also Wilkins et al. 2016), red [3.6]–[4.5] colors, and observed sizes (Holwerda et al. 2015; Shibuya et al. 2015) similar to the first samples of particularly luminous $z \sim 9$–10 galaxies identified by Oesch et al. (2014).
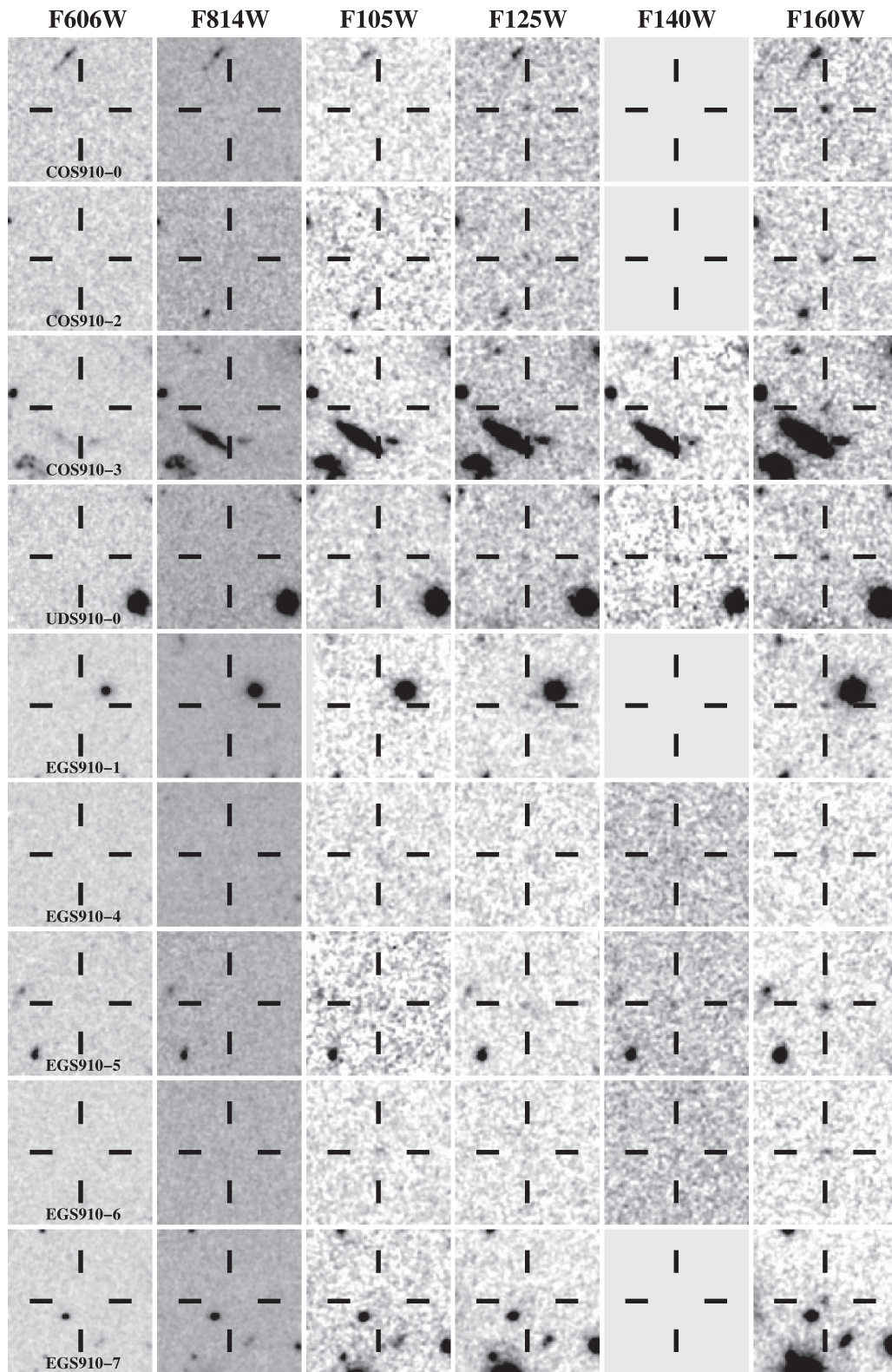
Figure 12. *HST + Spitzer*/IRAC images for 7 targeted candidate $z \sim 9$–10 galaxies which follow-up observations from our *HST* z9-CANDELS program failed to confirm as probable $z \geqslant 9$ galaxies using *HST* follow-up observations with our z9-CANDELS program. F105W-band observations were also obtained for the sources shown in the lowest two rows of this figure from the z9-CANDELS *HST* program. While neither source was explicitly targeted for observations by our program due to a relatively low prior probability of being at $z > 8$, we could not rule out that possibility, and so took advantage of the new data to gain more insight into their nature.

Figure 13. (Left) Best-fit SED models to the observed *HST*+*Spitzer*/IRAC+ground-based photometry for seven targeted candidate $z \sim 9$–10 galaxies (COS910-0, COS910-2, COS910-3, EGS910-1, EGS910-4, EGS910-5) which were not confirmed as probable $z > 8.4$ galaxies using follow-up observations from the z9-CANDELS program. The points and lines are otherwise as in Figure 4. F105W-band observations were also obtained for the sources shown in the lowest two rows of this figure (EGS910-6 and EGS910-7). While neither source was explicitly targeted for observations by our program due to a relatively low prior probability of being at $z > 8$, we could not rule out that possibility and so took advantage of the new data to gain more insight into their nature. (Right) Redshift likelihood distribution for these $z \sim 9$–10 candidates incorporating both our follow-up observations with *HST* and the *HST*+*Spitzer*/IRAC+ground-based observations that were used in the preselection (solid lines).

APPENDIX B
TARGETED $z \sim 9$–10 CANDIDATES THAT ARE MOST
LIKELY AT $z < 8.4$

A fraction of the candidate $z \sim 9$–10 galaxies targeted by our follow-up observations from the z9-CANDELS program appear not to be at $z > 8$. In Figure 12, we present postage stamps for 9 such sources (7 explicitly targeted by our program and 2 lower-probability $z \sim 9$–10 candidates which were incidentally targeted). In almost all of the candidates which are not confirmed by our follow-up observations, the sources show a $\geqslant 2\sigma$ detection in the Y_{105} band. Figure 13 shows the best-fit SED models for the tentative $z \sim 9$–10 galaxies that were not confirmed by observations from our follow-up program.

Detailed comments on specific candidate $z \sim 9$–10 galaxy that were targeted for follow-up with our z9-CANDELS program can be found below.

COS910-0: Follow-up of COS910-0 in the Y_{105} band shows a 3σ detection at 1.05 μm. A detailed fit to its SED suggests that it is actually a star-forming galaxy at $z = 7.8$. Its inclusion in our original sample of $z > 8.4$ candidate galaxies occurred due to its measured $J_{125} - H_{160}$ color, which was likely redder than reality due to the impact of noise.

COS910-2: COS910-2 is detected at 2.2σ in the Y_{105}-band follow-up observations. Such a detection is not expected if the galaxy is actually at $z \gtrsim 9$, and so the source must have a

19

F606W	F814W	F125W	F140W	F160W	[3.6]	[4.5]
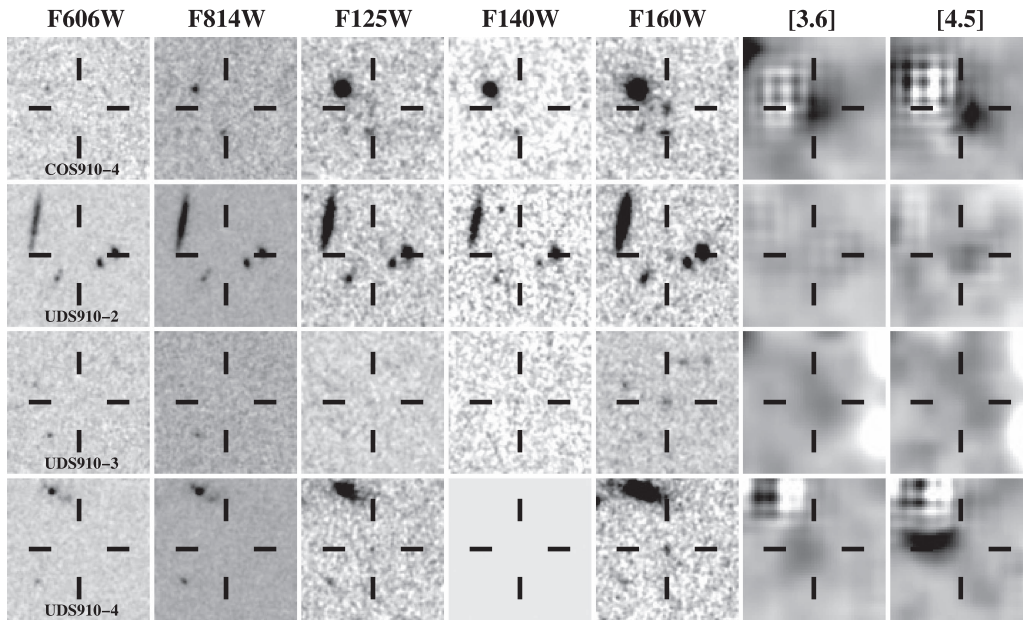
Figure 14. *HST* + *Spitzer*/IRAC images (6″ × 6″) of 4 possible $z \sim 9$–10 candidate galaxies that did not meet our criteria for preselection and hence were not targeted by our z9-CANDELS program. Sources are shown in the same passbands, as in Figure 10. None of these sources is explicitly targeted with our z9-CANDELS follow-up program.

Table 7
Possible $z \sim 9$–10 Galaxies over the CANDELS UDS, COSMOS, and EGS Program that Did Not Satisfy Our Criteria for Preselection and Hence Were Not Targeted for Follow-up Observations

ID	R.A.	decl.	$H_{160,AB}$	z_{phot}	$P(z > 8)$[a]
COS910-4	10:00:15.52	02:17:01.5	25.6 ± 0.1	9.3	0.18
UDS910-2[b]	02:17:13.08	−05:15:55.4	26.6 ± 0.2	10.2	0.68
UDS910-3	02:17:52.38	−05:15:06.3	26.9 ± 0.2	9.4	0.28
UDS910-4	02:17:14.61	−05:15:15.7	26.6 ± 0.2	9.1	0.50

Notes.
[a] Redshift likelihood is computed using the flux measurements for these sources in all photometric bands shown in Table 1.
[b] While the source UDS910-2 nominally has >50% probability of lying at $z > 8$, it was not targeted with our follow-up program z9-CANDELS because it could not be confirmed to be >90% probability candidate with the addition of a single orbit of *HST* observations.

redshift of $z \lesssim 8$. It may correspond to either a $z \sim 0.5$ or a $z \sim 8$ galaxy.

COS910-3: Follow-up of COS910-2 in the Y_{105} band and the JH_{140} band (1/3 of an orbit) shows a 1σ detection at 1.05 μm and 2σ detection in the JH_{140} band. Perhaps most importantly, the deeper photometry over the source in the JH_{140} band confirms that the source has a $JH_{140} - H_{160}$ color of 1.25 mag. While this is consistent with the source having a redshift of $z \gtrsim 11$, one would not expect to detect the source at 2σ in the J_{125} band in this case. These results suggest that the apparent break in the spectrum at 1.5 μm is not especially sharp and that this source shows faint but detectable flux to much bluer wavelengths.

UDS910-0: Follow-up of UDS910-0 in the Y_{105} band shows a 4σ detection at 1.05 μm. Therefore, this source cannot plausibly correspond to a $z \gtrsim 8.4$ galaxy. The best-fit redshift we compute for the source is $z \sim 7$. Like COS910-0, its inclusion in our sample of $z \sim 9$–10 galaxies likely occurred as a result of noise in the measured $J_{125} - H_{160}$ color.

EGS910-1: Follow-up of EGS910-1 in the Y_{105} band shows a 3σ detection at 1.05 μm, consistent with a redshift of $z < 8$.

EGS910-4: Follow-up of EGS910-4 in the Y_{105} band shows a 3σ detection at 1.05 μm, consistent with a redshift of $z < 8$.

EGS910-5: Follow-up of EGS910-5 in the Y_{105} band shows a 1.7σ detection at 1.05 μm, strongly suggesting that it is not at $z > 8$.

EGS910-6: EGS910-6 is detected at 4.5σ in our Y_{105}-band follow-up observations at 1.05 μm, providing clear evidence that it is at $z < 8$. A $z < 8$ solution is preferred at 99.8% confidence (Figure 13).

EGS910-7: Follow-up of EGS910-7 in the Y_{105} band only shows a 1.1σ detection at 1.05 μm. However, the $H_{160} - [3.6]$ color is sufficiently red that it seems more consistent with a lower-redshift galaxy than a $z > 8$ galaxy. The nature of this source is unclear.

APPENDIX C
OTHER CANDIDATE $z \sim 9$–10 GALAXIES OVER THE CANDELS-UDS, COSMOS, AND EGS FIELDS

When putting together a compilation of the most promising $z \sim 9$–10 candidates to target with follow-up *HST* observations,
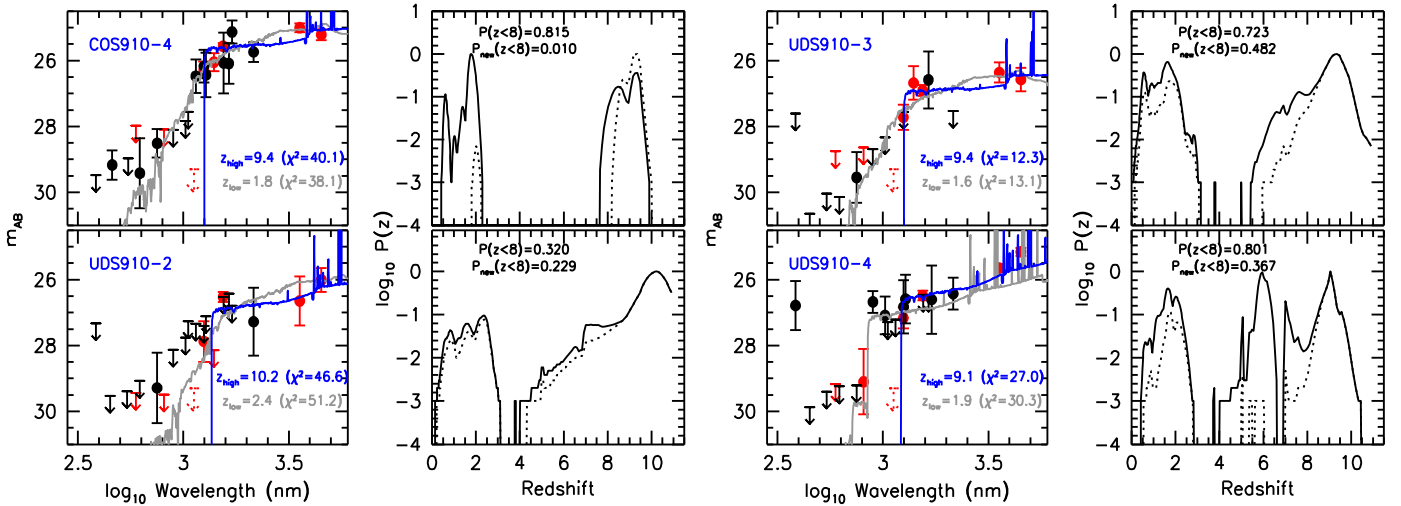
Figure 15. (Left) Best-fit SED models to the observed $HST+Spitzer$/IRAC+ground-based photometry of 4 possible $z \sim 9$–10 candidate galxies that did not meet our criteria for preselection and hence were not targeted by our z9-CANDELS follow-up program. Symbols are as in Figures 4 and 11. (Right) Redshift likelihood distribution for these 6 $z \sim 9$–10 candidates.

we experimented with a variety of different procedures to identify possible $z \sim 9$–10 galaxy candidates. As a result, we identified a larger number of possible $z = 9$–10 galaxy candidates than we could thoroughly follow-up with the 11 orbits allocated to our HST program.

While the redshift likelihood distributions we derived for these candidates suggested that the vast majority of them likely corresponded to sources at $z < 8$, it is nevertheless possible that several of these candidates might have redshifts in excess of $z \sim 8$.

We provide a short list of the "lower-probability" $z \sim 9$–10 galaxy candidates we identified over the CANDELS COS-MOS, UDS, and EGS fields in Table 7. These sources did not meet our criteria for preselection, but nevertheless may correspond to $z \sim 9$–10 galaxies. Figure 14 shows postage stamp cut-outs of these sources, while Figure 15 illustrates fits to their spectral energy distributions and our derived redshift likelihood contours for these sources.

REFERENCES

Anders, P., & Fritze-v. Alvensleben, U. 2003, A&A, 401, 1063
Ashby, M. L. N., Willner, S. P., Fazio, G. G., et al. 2013, ApJ, 769, 80
Ashby, M. L. N., Willner, S. P., Fazio, G. G., et al. 2015, ApJS, 218, 33
Atek, H., Richard, J., Kneib, J.-P., et al. 2014, ApJ, 786, 60
Atek, H., Richard, J., Kneib, J.-P., et al. 2015, ApJ, 800, 18
Barger, A. J., Cowie, L. L., & Wang, W.-H. 2008, ApJ, 689, 687
Barone-Nugent, R. L., Wyithe, J. S. B., Trenti, M., et al. 2015, MNRAS, 450, 1224
Beckwith, S. V. W., Stiavelli, M., Koekemoer, A. M., et al. 2006, AJ, 132, 1729
Bertin, E., & Arnouts, S. 1996, A&AS, 117, 39
Bielby, R., Hudelot, P., McCracken, H. J., et al. 2012, A&A, 545, AA23
Bouwens, R. 2014, HST Proposal, 13792
Bouwens, R., Bradley, L., Zitrin, A., et al. 2014a, ApJ, 795, 126
Bouwens, R. J., Illingworth, G. D., Franx, M., & Ford, H. 2007, ApJ, 670, 928
Bouwens, R. J., Illingworth, G. D., Franx, M., & Ford, H. 2008, ApJ, 686, 230
Bouwens, R. J., Illingworth, G. D., González, V., et al. 2010, ApJ, 725, 1587
Bouwens, R. J., Illingworth, G. D., Labbé, I., et al. 2011a, Natur, 469, 504
Bouwens, R. J., Illingworth, G. D., Oesch, P. A., et al. 2011b, ApJ, 737, 90
Bouwens, R. J., Illingworth, G. D., Oesch, P. A., et al. 2012, ApJ, 754, 83
Bouwens, R. J., Illingworth, G. D., Oesch, P. A., et al. 2014b, ApJ, 793, 115
Bouwens, R. J., Illingworth, G. D., Oesch, P. A., et al. 2015, ApJ, 803, 34
Bowler, R. A. A., Dunlop, J. S., McLure, R. J., et al. 2014, MNRAS, 440, 2810
Bowler, R. A. A., Dunlop, J. S., McLure, R. J., et al. 2015, MNRAS, 452, 1817
Brammer, G. B., van Dokkum, P. G., & Coppi, P. 2008, ApJ, 686, 1503
Brammer, G. B., van Dokkum, P. G., Franx, M., et al. 2012, ApJS, 200, 13

Castellano, M., Fontana, A., Grazian, A., et al. 2012, A&A, 540, A39
Cirasuolo, M., McLure, R. J., Dunlop, J. S., et al. 2010, MNRAS, 401, 1166
Coe, D., Bradley, L., & Zitrin, A. 2015, ApJ, 800, 84
Coe, D., Zitrin, A., Carrasco, M., et al. 2013, ApJ, 762, 32
Dressel, L., et al. 2012, Wide Field Camera 3 Instrument Handbook, Version 5.0 (Baltimore: STScI)
Ellis, R. S., McLure, R. J., Dunlop, J. S., et al. 2013, ApJL, 763, L7
Fialkov, A., & Loeb, A. 2015, ApJ, 806, 256
Finkelstein, S. L., Papovich, C., Salmon, B., et al. 2012, ApJ, 756, 164
Finkelstein, S. L., Ryan, R. E., Jr., Papovich, C., et al. 2015, ApJ, 810, 71
Fontana, A., Dunlop, J. S., Paris, D., et al. 2014, A&A, 570, AA11
Furusawa, H., Kosugi, G., Akiyama, M., et al. 2008, ApJS, 176, 1
Grogin, N. A., Kocevski, D. D., Faber, S. M., et al. 2011, ApJS, 197, 35
Holwerda, B. W., Bouwens, R., Oesch, P., et al. 2015, ApJ, 808, 6
Illingworth, G. D., Magee, D., Oesch, P. A., et al. 2013, ApJS, 209, 6
Ishigaki, M., Kawamata, R., Ouchi, M., et al. 2015, ApJ, 799, 12
Kawamata, R., Ishigaki, M., Shimasaku, K., Oguri, M., & Ouchi, M. 2015, ApJ, 804, 103
Koekemoer, A. M., Faber, S. M., Ferguson, H. C., et al. 2011, ApJS, 197, 36
Kotulla, R., Fritze, U., Weilbacher, P., & Anders, P. 2009, MNRAS, 396, 462
Kron, R. G. 1980, ApJS, 43, 305
Labbé, I., Bouwens, R., Illingworth, G. D., & Franx, M. 2006, ApJL, 649, L67
Labbé, I., Oesch, P. A., Illingworth, G. D., et al. 2015, ApJS, 221, 23
Labbé, I., Oesch, P. A., Bouwens, R. J., et al. 2013, ApJL, 777, L19
Labbé, I., González, V., Bouwens, R. J., et al. 2010a, ApJL, 708, L26
Labbé, I., González, V., Bouwens, R. J., et al. 2010b, ApJL, 716, L103
Lotz, J., Mountain, M., Grogin, N. A., et al. 2014, in AAS Meeting 223 Abstracts, 254.01
Mason, C. A., Treu, T., Schmidt, K. B., et al. 2015, ApJ, 805, 79
McCracken, H. J., Capak, P., Salvato, M., et al. 2010, ApJ, 708, 202
McCracken, H. J., Milvang-Jensen, B., Dunlop, J., et al. 2012, A&A, 544, A156
McLeod, D. J., McLure, R. J., Dunlop, J. S., et al. 2015, MNRAS, 450, 3032
McLure, R. J., Dunlop, J. S., Bowler, R. A. A., et al. 2013, MNRAS, 432, 2696
Oesch, P. A., Bouwens, R. J., Carollo, C. M., et al. 2010, ApJL, 709, L21
Oesch, P. A., Bouwens, R. J., Illingworth, G. D., et al. 2012, ApJ, 745, 110
Oesch, P. A., Bouwens, R. J., Illingworth, G. D., et al. 2013, ApJ, 773, 75
Oesch, P. A., Bouwens, R. J., Illingworth, G. D., et al. 2014, ApJ, 786, 108
Oesch, P. A., Bouwens, R. J., Illingworth, G. D., et al. 2015, ApJ, 808, 104
Oesch, P. A., Brammer, G., van Dokkum, P. G., et al. 2016, ApJ, 819, 129
Oke, J. B., & Gunn, J. E. 1983, ApJ, 266, 713
Ono, Y., Ouchi, M., Curtis-Lake, E., et al. 2013, ApJ, 777, 155
Postman, M., Coe, D., Benítez, N., et al. 2012, ApJS, 199, 25
Roberts-Borsani, G. W., Bouwens, R. J., Oesch, P. A., et al. 2016, ApJ, 823, 143
Rogers, A. B., McLure, R. J., Dunlop, J. S., et al. 2014, MNRAS, 440, 3714
Shibuya, T., Ouchi, M., & Harikane, Y. 2015, ApJ, 219, 15
Skelton, R. E., Whitaker, K. E., Momcheva, I. G., et al. 2014, ApJS, 214, 24

Smit, R., Bouwens, R. J., Labb, Ì., et al. 2014, ApJ, 784, 58

Smit, R., Bouwens, R. J., Franx, M., et al. 2015, ApJ, 801, 122

Steidel, C. C., Adelberger, K. L., Giavalisco, M., Dickinson, M., & Pettini, M. 1999, ApJ, 519, 1

Trenti, M. 2014, HST Proposal, 13767

Trenti, M., & Stiavelli, M. 2008, ApJ, 676, 767

Weiner, B. J. & AGHAST Team 2014, in AAS Meeting 223 Abstracts, 227.07

Wilkins, S. M., Bouwens, R. J., Oesch, P. A., et al. 2016, MNRAS, 455, 659

Wilkins, S. M., Bunker, A. J., Stanway, E., Lorenzoni, S., & Caruana, J. 2011, MNRAS, 417, 717

Willott, C. J., McLure, R. J., Hibon, P., et al. 2013, AJ, 145, 4

Windhorst, R. A., Cohen, S. H., Hathi, N. P., et al. 2011, ApJS, 193, 27

Wyithe, J. S. B., Yan, H., Windhorst, R. A., & Mao, S. 2011, Natur, 469, 181

Zheng, W., Postman, M., Zitrin, A., et al. 2012, Natur, 489, 406 (Z12)

Zheng, W., Shu, X., Moustakas, J., et al. 2014, ApJ, 795, 93

Zitrin, A., Labbé, I., Belli, S., et al. 2015, ApJL, 810, L12

Zitrin, A., Zheng, W., Broadhurst, T., et al. 2014, ApJL, 793, L12